**Atmospheric
Chemistry
and Physics**

Aerosol direct radiative effect in the Po Valley region derived from AERONET measurements

M. Clerici and F. Mélin

European Commission – DG Joint Research Centre, Institute for Environment and Sustainability, Global Environment Monitoring Unit, TP272, Ispra, 21020, Italy

Abstract. The aerosol direct radiative effect (ADRE) affecting the Po Valley and the adjacent North Adriatic Sea is studied using 10-year series of measurements collected at two AERONET sites located in the western part of the Valley (Ispra), and on a platform (AAOT) offshore Venice. This region is characterized by a high, mostly continental, aerosol load with comparable average aerosol optical thickness τ_a at both locations (0.21 at 500 nm) and more absorbing aerosols at Ispra. A dynamic aerosol model accounting for the changes in scattering phase function with τ_a is used for radiative transfer calculations, together with boundary conditions representative of terrestrial and marine surfaces. A sensitivity analysis allows the construction of an error budget for the daily ADRE estimates, found to be of the order of 20% and mostly due to uncertainties on aerosol single scattering albedo and τ_a. The daily radiative efficiencies, normalized by τ_a at 500 nm, increase from December to June, from -17 to $-24\,\mathrm{W\,m^{-2}}\,\tau_a^{-1}$ at top-of-atmosphere (TOA) and -33 to $-72\,\mathrm{W\,m^{-2}}\,\tau_a^{-1}$ at surface for the Po Valley, and from -15 to -32 (TOA) and -35 to $-65\,\mathrm{W\,m^{-2}}\,\tau_a^{-1}$ (surface) for the AAOT site. The average of log-transformed ADRE for TOA, surface and atmosphere are -5.2, -12.2 and $+6.8\,\mathrm{W\,m^{-2}}$ for the Po Valley case, and -6.5, -13.0 and $+6.5\,\mathrm{W\,m^{-2}}$ for the AAOT site but these values can be much higher for individual days. Concurrent clear-sky days give indications on the regional atmospheric heating spatial gradients. Differences between the atmospheric ADRE at the two locations average $6.3\,\mathrm{W\,m^{-2}}$ with a gradient positive towards the inner valley in 65% of the cases. This study confirms the importance of duly considering the radiative impact of aerosols on the regional climate.

1 Introduction

Aerosols have an impact on the radiative budget and hydrological cycle of the Earth through a variety of processes (Charlson et al., 1992; Ramanathan et al., 2001). A direct action is by the scattering and absorption of solar radiation, the latter in turn reducing cloud cover by heating the lower atmosphere (the semi-direct effect, Hansen et al., 1997). Moreover, by affecting cloud microphysical properties and lifetime, the aerosol particle distribution further affects the planetary albedo and precipitation patterns (Lohmann and Feichter, 2005; Rosenfeld, 2000). This overall impact is now widely recognized for global studies but the uncertainties associated with the aerosol effects remain higher than those associated with greenhouse gases (IPCC, 2001). A factor contributing to these uncertainties is the temporal and geographic variability of aerosols and their properties that partly explains the large diversity of published estimates (Yu et al., 2006). Particularly, the spatial gradients of the radiative effect of aerosols are much higher than those of greenhouse gases (Matsui and Pielke, 2006) and logically, several studies have focused on how aerosols may affect regional climates in areas of intense sources (e.g., Menon et al., 2002; Chung et al., 2002; Lau et al., 2006).

In Europe, the Po Valley (northern Italy) is a densely populated region, with intense rural and industrial activities, that stands out in regional maps of aerosol load (Chu et al., 2003; Barnaba and Gobbi, 2004) or emitted gases like NO_2 (Beirle et al., 2004). Besides the concerns for air quality and health, studies of aerosols are needed for an accurate characterization of the radiative budget of the area. The present contribution is based on two 10-year time series of sun-photometer measurements that serve for radiative transfer computations and for the estimation of the aerosol direct radiative effect (ADRE). The two sites, separated by approximately 300 km, are adequately situated at two ends of the Valley, and provide measurements covering diurnal to inter-annual time scales.

Correspondence to: M. Clerici
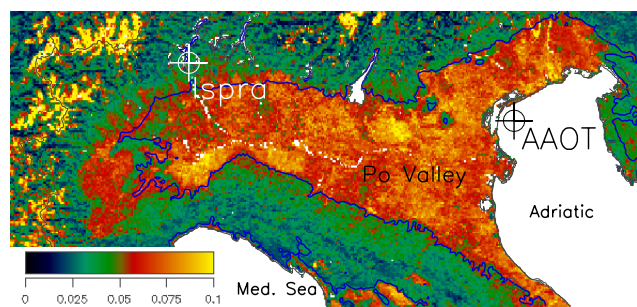(marco.clerici@jrc.it)

Fig. 1. Map of northern Italy, with the locations of the two AERONET sites of AAOT and Ispra. The background distribution is the 2003 annual average white-sky MODIS albedo (spectrally integrated for the 0.3–0.7 μm domain). The blue line represents the 200-m elevation level, delineating the region of interest.

Interestingly, one site is located offshore in the coastal area of the northern Adriatic Sea and thus offers the opportunity to analyze the differences caused by different surface boundary conditions.

The main objective of the study is to quantify the aerosol direct radiative effect for the region at temporal scales from instantaneous to seasonal. The aerosol data are first described, and a comparative analysis of the direct radiative effect is performed for atmospheric and surface conditions characteristic of the two sites. Then, an assessment of the ADRE accuracy is performed taking into account different sources of error, related to the definition of the optical properties of the atmosphere-surface system and to methodological approximations. Finally, the daily to seasonal estimates of the aerosol direct radiative effect are presented.

2　Data and methods

2.1　Description of the sites and data

The study is based on measurements collected at two sites located at two ends of the Po Valley in northern Italy (Fig. 1). One site is in the precincts of the Joint Research Centre (45°48′ N, 08°37′ E, elevation 235 m), close to Ispra, a village 55 km northwest of Milan and 16 km west of Varese. This location is surrounded by villages, fields, forests and lakes. The second site is the Acqua Alta Oceanographic Tower (AAOT), located in the Adriatic Sea, 15 km off the Venice lagoon (45°19′ N, 12°30′ E). The Po Valley has a flat topography surrounded by mountains (Alps and Apennines) and closed on the eastern side by the Adriatic Sea. Regional aerosol sources include large industrial, urban and rural emissions; air mass advection can also bring aerosols from the Mediterranean basin (with rare Saharan dust inputs; Rodríguez et al., 2007a) or from more northern European regions (e.g., Sogacheva et al., 2007). These conditions, together with low average levels of windiness (Rodríguez et al.,

2007b), favor high loads of particles and pollutants (Van Dingenen et al., 2004; Beirle et al., 2004) and a relative homogeneity at the scale of the valley (Mélin and Zibordi, 2005). Information on chemical analyzes of Po Valley aerosols can be found in Matta et al. (2003) or Putaud et al. (2002, 2004).

Both measurement sites are part of the Aerosol Robotic Network (AERONET) (Holben et al., 1998). The instruments, CE-318 automated sun-photometers (CIMEL, Paris, France), have recorded radiometric data at the center wavelengths 440, 500, 675, 870, 940 and 1020 nm since August 1996 and July 1997 at the AAOT site and Ispra, respectively. Exceptions are the wavelength 500 nm not recorded at AAOT before July 1997 and at Ispra before February 2001, and an interruption in the Ispra time series between October 1998 and May 1999. The additional wavelengths at 412 and 555 nm are available after November 2001 at the AAOT site.

The direct solar irradiance measurements are used to derive the aerosol spectral optical thickness $\tau_a(\lambda)$ at the associated wavelength λ through the Beer-Lambert-Bouguer law. The wavelength 940 nm is used only for the calculation of the amount of precipitable water vapor. The processing of the data is described by Holben et al. (1998) and Smirnov et al. (2000) (AERONET Version 2 direct Sun algorithm). Additionally, the Ångström exponent α has been computed by linear regression, as a function of wavelength, of the log-transformed τ_a between 440 and 870 nm (3 or 4 wavelengths). All the data are so-called Level 2 according to the cloud-screening and quality control from AERONET (Smirnov et al., 2000). An exception is the period at the AAOT before June 1999, that is considered Level 1.5 (the final step of quality assurance missing). The expected accuracy for the aerosol optical thickness is 0.015 (Eck et al., 1999). A daily value is computed as the average of all measurements recorded during the day if at least three measurements are available.

Additional information is used for a more comprehensive characterization of the aerosol properties at the two sites: the single scattering albedo ω_a, the asymmetry factor g_a, the scattering phase function ψ_a at 440, 670, 870 and 1020 nm, and the volume particle size distribution VSD. These estimates result from the AERONET Version 1 direct Sun and almucantar inversion algorithms (Dubovik and King, 2000) and are available for the periods June 1999 to December 2005 at the AAOT site, and July 1997 to November 2005 at Ispra. The inversions are based on the assumption of homogeneous spherical aerosols. In the case of aerosols dominated by fine particles (as for the considered sites, see below), the uncertainties for these inversions are estimated to be 0.03 for ω_a, 15% to 25% for the VSD in the radius range 0.1 to 7 μm and 25% to 100% for the tails of the size distribution (Dubovik et al., 2000).

The main optical properties of aerosols have been presented for these sites by Mélin and Zibordi (2005), and more completely for the AAOT site by Mélin et al. (2006). They are here briefly recalled and updated. The frequency
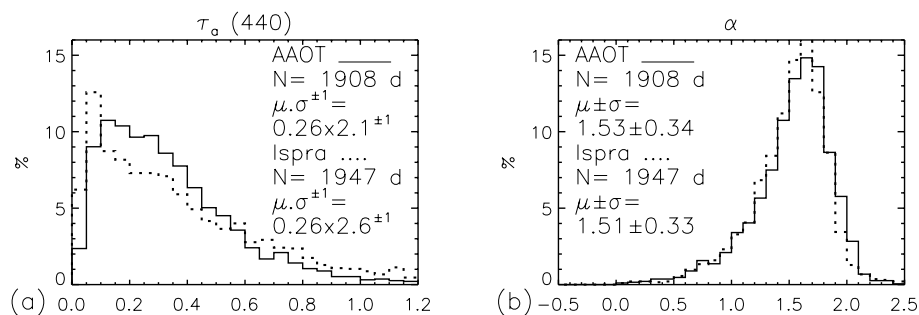
Fig. 2. Frequency distributions of the daily aerosol (**a**) optical thickness, τ_a, at 440 nm, and (**b**) Ångström exponent, α. N, μ, and σ are the number of days, the overall mean, and the standard deviation of the distributions, respectively. For τ_a, log-transformed statistics are presented (the arithmetic mean and standard deviation for $\tau_a(440)$ are 0.34±0.23 and 0.37±0.29 for AAOT and Ispra, respectively.)

distributions of the aerosol optical thickness τ_a at 440 nm (selected because this wavelength is available for the entire measurement record at both sites) and the Ångström exponent α are shown on Fig. 2, and a synthesis of the main optical properties is given in Table 1. The frequency distribution of the aerosol optical thickness is better approximated by a log-normal distribution than by a normal law, as proposed by O'Neill et al. (2000) and confirmed by Fig. 2 and by values of skewness and kurtosis, and thus log-transformed statistics are reported for τ_a. On the basis of N_d=1908 daily records at the AAOT site, τ_a averages 0.264 at 440 nm (0.221 at 500 nm with N_d=1840 daily records). For Ispra, these averages are 0.257 for $\tau_a(440)$ (N_d=1947) and 0.206 for $\tau_a(500)$ (N_d=1303). The average Ångström exponent is also found similar at both sites, 1.53±0.34 and 1.51±0.33 at AAOT and Ispra, respectively. The relatively high values of α underline the predominance of continental aerosols, in line with the sources defining the aerosol regime in the Po Valley. These aerosol optical characteristics also resemble those of sites located in a urban/industrial environment (Holben et al., 2001; Dubovik et al., 2002).

The statistical basis available for the inherent optical properties is much smaller (Table 1), with a number of data records at the AAOT site and Ispra, respectively amounting to 2627 and 2253 for g_a, ψ_a and VSD, and 797 and 727 for ω_a (these lower numbers are explained by the fact that the inversion algorithm does not return values for ω_a in cases of low value of τ_a). A similar spectral dependency can be noticed for both sites, with ω_a decreasing with wavelength, as mostly observed for aerosols other than dust (e.g., Dubovik et al., 2002), and g_a also decreasing with wavelength, consistent with a decrease in the scattering effective particle size (Hansen and Travis, 1974). The aerosols associated with the location of AAOT appear less absorbing on average; this might be due to a location farther from the main pollution sources and to a background marine component. These properties, in terms of amplitude and spectral dependence, are well in line with results published for other continental sites, even if the local sources might have dif-

Table 1. Overall statistics (average and standard deviation) for the aerosol optical thickness τ_a (log-transformed statistics), the Ångström exponent α, the single scattering albedo ω_a and the asymmetry factor g_a. Wavelengths are indicated in nm. For τ_a and α, the statistics are computed with the daily averages of the entire time series (see also Fig. 2); N_d is the number of days, with the value in brackets given for $\tau_a(500)$. The statistics for ω_a and g_a are computed over all N individual records.

Site	AAOT	Ispra
τ_a	N_d=1908(1840)	N_d=1947(1303)
440	$0.264 \times 2.11^{\pm 1}$	$0.257 \times 2.55^{\pm 1}$
500	$0.221 \times 2.15^{\pm 1}$	$0.206 \times 2.61^{\pm 1}$
675	$0.141 \times 2.21^{\pm 1}$	$0.137 \times 2.66^{\pm 1}$
870	$0.095 \times 2.22^{\pm 1}$	$0.094 \times 2.60^{\pm 1}$
α	1.53±0.34	1.51±0.33
ω_a	N=797	N=727
441	0.956±0.017	0.928±0.032
673	0.942±0.025	0.923±0.035
873	0.918±0.039	0.908±0.044
1022	0.906±0.047	0.898±0.051
g_a	N=2627	N=2253
441	0.691±0.032	0.691±0.046
673	0.626±0.049	0.606±0.055
873	0.595±0.050	0.564±0.053
1022	0.579±0.053	0.548±0.053

ferent charactistics. For instance, the average spectra of ω_a and g_a appear close to those reported at Greenbelt, Maryland, US, and Créteil-Paris, France (Dubovik et al. 2002, at these 2 sites ω_a decreases from 0.98 to 0.95 and from 0.94 to 0.91, respectively), or at Lecce, southeastern Italy (Perrone et al. 2005; 2 modes of the frequency distribution of $\omega_a(440)$ are there distinguished, centered at 0.94 and 0.974). It is however acknowledged that much lower values of ω_a can be found, particularly close to large cities, as reported for example in summer for the Marseille or Paris urban areas (respectively, $\omega_a(550)$ of 0.85±0.05, Mallet et al. 2003,
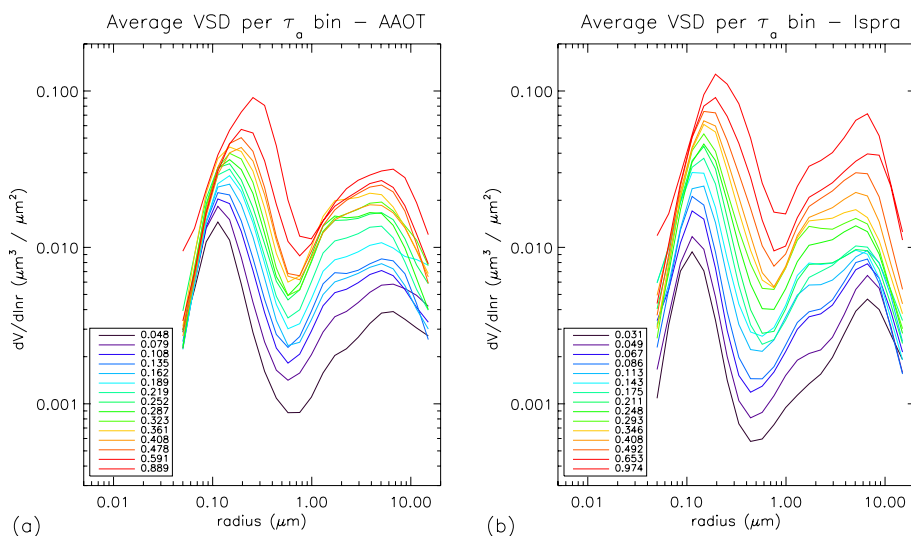
Fig. 3. Aerosol volume size distribution VSD averaged by bin of $\tau_a(500)$, for the AAOT **(a)** and Ispra **(b)** sites.

and $\omega_a(550)$ of 0.85–0.92, Chazette et al. 2005), or as annual mean for Valencia, Spain (ω_a of 0.90±0.05, Estellés et al. 2007).

The similarity between the optical properties found at the two locations also confirms the results presented by Mélin and Zibordi (2005). That study also showed a large degree of temporal correlation between the two time series at various time scales, from daily to monthly. Conversely, the mean diurnal cycle was found to be quite different. The diurnal variability exhibited at the Ispra site is similar to that documented for other sites influenced by urban/industrial centers (Smirnov et al., 2002), with an increase of τ_a amounting to ~10% on average between the mid-to-end morning and the end of the afternoon. Conversely, at the AAOT site the aerosol load is found to decrease from the early morning to the afternoon by an amplitude of 20% (annual average). The impact of this diurnal variability will be further addressed below in terms of aerosol radiative effect.

2.2 Definition of the aerosol model for each site

In a previous study (Mélin et al., 2006) and similarly to the work of Remer and Kaufman (1998), a relationship between aerosol optical properties and the particle volume size distribution has been illustrated for the AAOT site, and is now summarized and extended to the measurements collected at Ispra. Figure 3 represents the VSD averaged per interval of increasing τ_a at 500 nm, with 15 intervals of equal sample size for each data set. Three modes are apparent for the VSD, whose modal radius r_v can be computed assuming a combination of log-normal distributions. The positions of the modes associated with large particles are rather constant, 1.3 and 6.0 μm for both data sets (average over all bins). Conversely, the modal radius of the small particles (accumulation

mode) increases with the aerosol load, from 0.13 to 0.23 μm at the AAOT site, and from 0.12 to 0.22 μm at the Ispra site. This shift is associated with the growth of the small particles with humidity and is in line with the relationships found between precipitable water vapor and the amplitude and spectral shape of $\tau_a(\lambda)$ (see Mélin et al., 2006, for the AAOT site).

The aerosol scattering phase function ψ_a also displays an angular dependence as the aerosol load increases (Fig. 4). Thus for both sites, the peaks of forward and backward scattering decreases for large τ_a. The asymmetry factor g_a reflects this trend, increasing slightly with τ_a (for instance, the bin-averaged g_a at 440 nm approximately increases from 0.65 to 0.73 at both sites). The change in size distribution and water content is also translated in terms of single scattering albedo that tends to increase with τ_a. As indicated in the previous sub-section, valid values for ω_a from the inversion process are obtained only for the high range of aerosol loads; in practice, ω_a statistics are available for the last five bins, corresponding to $\tau_a(500)$ above approximately 0.3. Over this interval, the bin-averaged ω_a at 440 nm increases from 0.95 to 0.96 at the AAOT site, and from 0.92 to 0.95 at Ispra.

The clear relationship between τ_a and the aerosol physical (VSD) and inherent optical properties (ψ_a) allows the definition of an aerosol model for each site, whose optical properties evolve dynamically with τ_a and are used for performing radiative transfer (RT) simulations, as described in Sect. 2.4. This has the advantage of accounting for the dependence on the size distribution of the radiative effect (Kiehl and Briegleb, 1993). Considering a statistical basis restricted to the high range of τ_a, the spectrum of single scattering albedo is kept constant (values given in Table 1). From the four wavelengths available for ψ_a and ω_a, the spectrum of these optical properties is determined by extrapolation in the
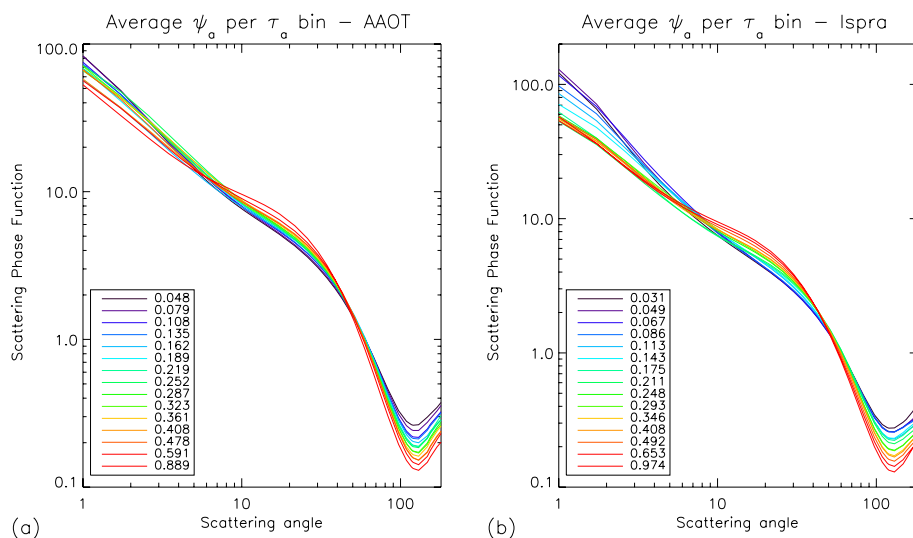
Fig. 4. Aerosol scattering phase function averaged by bin of $\tau_a(500)$, for the AAOT **(a)** and Ispra **(b)** sites.

range 0.25 to 2 μm. The uncertainties resulting from the extrapolation of the optical properties in the interval from 1 to 2 μm can be considered as relatively small for these types of aerosols (Haywood and Shine, 1995; Russel et al., 1999; Redemann et al., 2000).

2.3 Surface albedo

The radiative transfer simulations require the definition of the surface boundary conditions. Over marine surfaces, the boundary condition is represented by a bidirectional reflectance distribution function (BRDF) for water (see Mayer and Kylling, 2005), mainly depending on wind speed according to the wave slope distribution of Cox and Munk (1956).

Over land, the values of the albedo ρ are defined using the albedo product (collection 4) derived from the Moderate Resolution Imaging Spectroradiometer (MODIS, Salomonson et al., 1989) on board the Terra platform. This product is distributed as global maps (1-min spatial resolution) representing sixteen-day averages of the so-called black-sky and white-sky albedos for wavelengths centered at 0.47, 0.55, 0.67, 0.86, 1.24, 1.64, and 2.1 μm (Schaaf et al., 2002; Moody et al., 2005). The black-sky albedo corresponds to the directional hemispherical reflectance computed at solar noon, and the white-sky albedo to the bi-hemispherical reflectance in conditions of isotropic illumination. The first validation analyses state an absolute accuracy mostly within ±0.02 for the integrated shortwave albedo (Lucht et al., 2000; Jin et al., 2003). This satellite data set is not available for the entire AERONET record, and the albedo annual cycle is here defined by considering the year 2003 as representative.

Figure 1 displays the 2003 annual average albedo (white-sky product) spectrally integrated for the visible domain (0.3–0.7 μm). The Po Valley is easily distinguished by white-sky albedo values higher than approximately 0.05 and elevations lower than 200 m, the two thresholds matching remarkably well (the blue line on Fig. 1 thus encompasses the region of interest). This region is classified as cropland by the MODIS International Geosphere Biosphere Program ecosystem classification (Friedl et al., 2002), to which should be added the influence of large cities. The area in the immediate vicinity of Ispra is more rural and forested, with lower values of albedo. In order to analyze the aerosol radiative effect for the region, the albedo spectra averaged over a small area around Ispra (approximately 15 km) and over the whole Po Valley, defined by elevations lower than 200 m, are considered, and are shown on Fig. 5 as seasonal averages. White-sky and black-sky albedos are close, particularly for the spectral domain below 0.9 μm which is of primary interest for calculations of the aerosol radiative effect. The annual average white-sky albedo spectrally integrated in the domain 0.3–0.7 μm is 0.036 and 0.067 around Ispra and for the Valley, respectively. For the interval 0.7–5 μm, it is 0.200 and 0.250, respectively.

For the purpose of our study, the albedo used for the RT calculations is taken as the average of the noon white-sky and black-sky albedos weighted by the actual ratio of diffuse and direct irradiance. This takes into account the effect of the aerosol load on the geometry of the radiance field. The variations during the day with respect to the values at noon of the two albedo components are ignored, but the moderate dependence on the solar zenith angle should introduce small errors on the radiative effect, particularly for daily or monthly averages (Yu et al., 2004). Radiative transfer calculations are performed with the two types of surfaces and associated albedo values (Ispra and Po Valley). Differences between the results obtained by these two sets of calculations can be
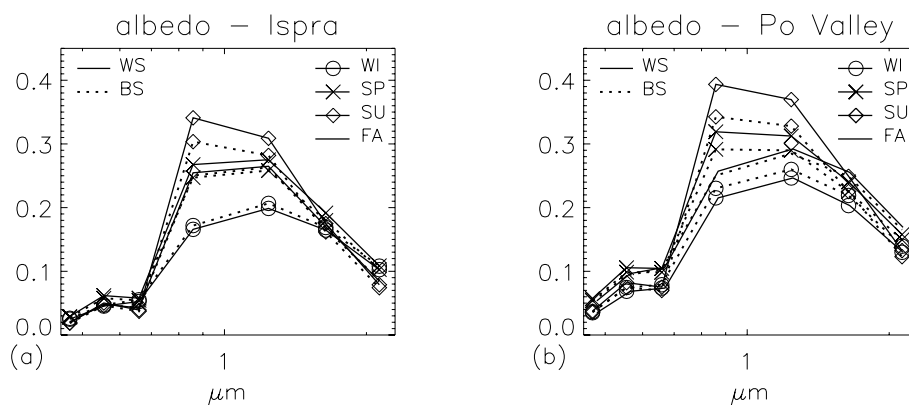
Fig. 5. Seasonal means of MODIS albedo spectrum averaged for the Ispra area **(a)** and the Po Valley region **(b)**, as limited by the 200-m elevation line. WS and BS stand for white-sky and black-sky, respectively. WI, SP, SU, and FA stand for the winter, spring, summer and fall seasons.

considered to assess the dependence on the albedo values as well as their associated uncertainties, including the intrinsic uncertainty of the product, the residual dependence on the solar zenith angle, or the possible impact of the inter-annual variability of the regional albedo.

For the sake of completeness, an albedo spectrum of uniformly snow-covered surfaces from the ASTER Spectral Library (Medium Granular Snow) is considered to assess the impact on ADRE of highly reflecting surfaces. These conditions are extreme for the Po Valley, where snow events are unfrequent (for instance at Ispra, in the pre-alpine part of the Valley, snow falls occurred just a few days per year in the last decade), and the properties of the ground at the scale of tens of kilometer are usually different from these snow simulations, because of heterogeneity of the snow cover remaining after snow fall. Snow cases are not specfically included into the time series presented in Sect. 4.

2.4 Radiative transfer calculations

The radiative budget with and without aerosols is determined using the libRadtran package (see Mayer and Kylling, 2005, for a complete overview) and applying the DISORT2 code for the radiative transfer computations (Stamnes et al., 1998). The solar irradiance spectrum is from Kurucz (1992) with a spectral resolution of 0.1 nm. The standard US 1976 atmospheric profile (Anderson et al., 1986) is assumed for gas absorption and scattering, modelled over 50 plane parallel layers ranging from the surface up to 120 km; the use of a different profile will impact the aerosol radiative effect within a few percent (Boucher and Tanré, 2000; Bellouin et al., 2003). The SBDART k-correlated parametrization is used for gas absorption in the near-infrared (Ricchiazzi et al., 1998). The aerosol load is homogeneously distributed in the lower troposphere, up to 3 km, and the optical properties are represented by the single scattering albedo and the Legendre expansion of the scattering phase function. The importance of a proper

representation of the aerosol scattering phase function in determining the radiative effects has been recognized in previous studies (e.g., Boucher, 1998a), so that a high number of coefficients (1000) of the Legendre expansion is selected to guarantee the accuracy of the phase function representation.

For the AAOT site, a BRDF for water surfaces is selected (Mayer and Kylling, 2005), with a wind speed of $2\,\mathrm{m\,s^{-1}}$ well representative of the average local meteorological conditions. Previous analyses, performed with a coupled water-atmosphere code, demonstrated that changes in the water content and its bio-optical properties do not result in significant changes in the radiative effect. An increase of the background chlorophyll a concentration from 0.05 to $1.0\,\mathrm{mg\,m^{-3}}$ affects the ADRE by only 0.6% and 0.3% at the top-of-atmosphere and surface, respectively (Mélin et al., 2006). For terrestrial surfaces, a lambertian surface with albedo ranging from 0.02 to 0.5 (12 values) is assumed for calculations performed with the Ispra aerosol model. An additional configuration is considered by combining this aerosol model with the water BRDF, in order to separate the effect of the aerosol and surface properties on the radiative fluxes (see Sect. 3.1).

In practice, radiative transfer computations are performed with the aerosol models associated with each τ_a bin (Sect. 2.2), for every wavelength λ and solar zenith angle θ_0 in the range $20°$ (lowest value at this latitude) to $85°$ (by steps of $5°$), and for the range of albedo values. The results are stored into a look-up table (LUT) for following analysis and representation of the results. As recalled previously, the Po Valley is characterized by a relative homogeneity of the aerosol properties and variability (see Sect. 2.1 and Mélin and Zibordi, 2005). Thus, in the standard RT calculations, the aerosol characteristics at Ispra are taken as representative of at least the inner Valley and are used for radiative simulations over land, whereas the aerosol characteristics associated with AAOT are used for calculations over the Adriatic
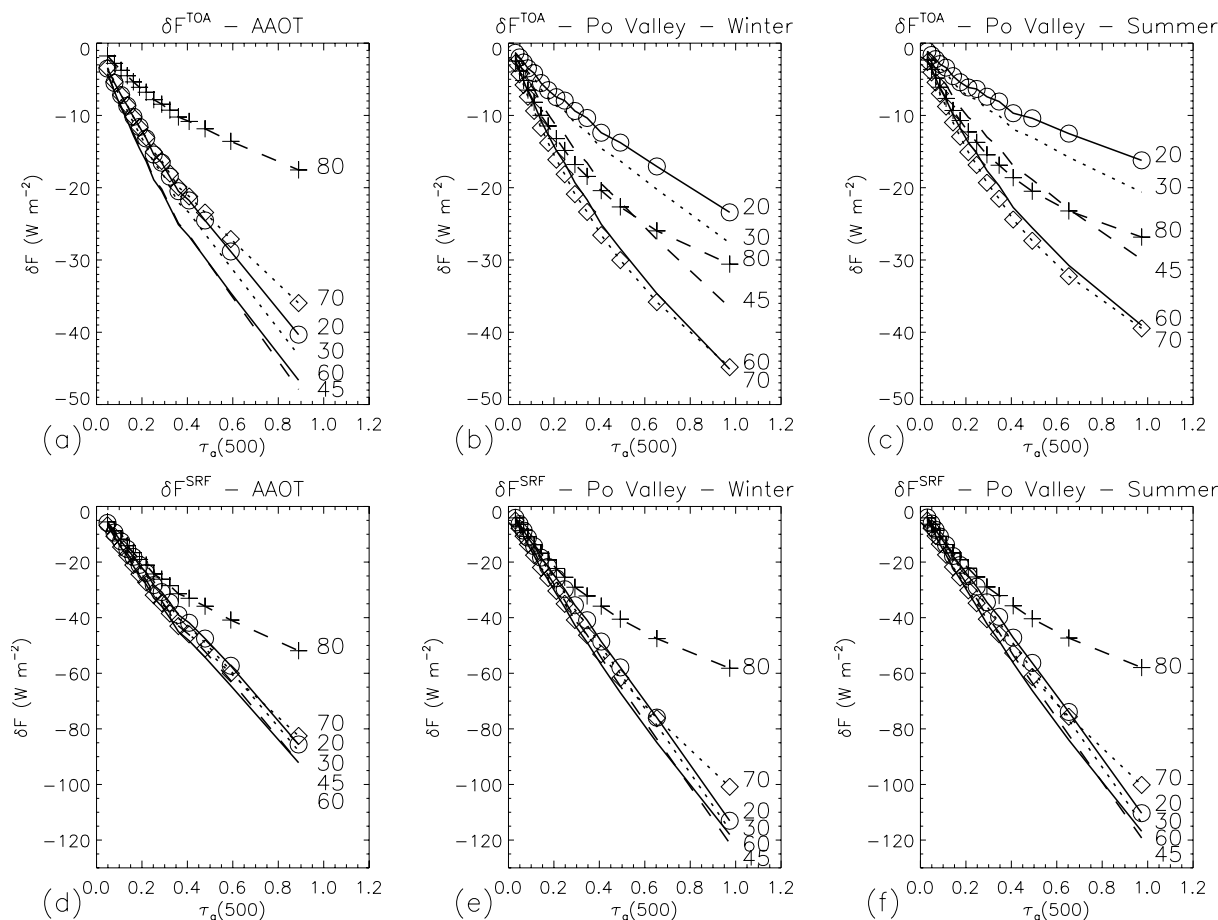
Fig. 6. Top-of-atmosphere **(a), (b), (c)** and surface **(d), (e), (f)** instantaneous aerosol direct radiative effect δF as a function of τ_a for the AAOT site (a), (d), and the Po Valley in winter (b), (e) and summer (c), (f). The numbers associated with each curve is the solar zenith angle.

Sea. For sensitivity analyses, a reference case is defined by selecting the bins whose average τ_a is close to the overall average, τ_a=0.211 for Ispra (8th bin), and τ_a=0.219 for AAOT (7th bin).

First, the instantaneous radiative effect (spectrally resolved or integrated) associated with one τ_a bin is derived directly from the LUT for the top-of-atmosphere (TOA) as $\delta F^{TOA}(\tau_a)$, expressed by the difference of the diffuse upward irradiance with and without aerosol, and for the surface, as $\delta F^{SRF}(\tau_a)$ obtained by subtracting the total downward irradiance in presence of aerosol from that computed for an aerosol free atmosphere. For given τ_a and θ_0, δF is obtained from the LUT by bilinear interpolation. For terrestrial surfaces, the albedo spectrum typical of each season (Fig. 5) is selected, with values for a specific wavelength λ obtained by interpolation between the MODIS channels. Subsequently δF can be integrated in time at daily to seasonal scales to analyze the time series of the clear-sky aerosol direct radiative effect.

3 Comparative analysis and uncertainties

3.1 Comparative analysis

This section describes the characteristics of the aerosol direct radiative effect (ADRE) for sites representative of the Po Valley and the adjacent sea, particularly its variations with the aerosol optical thickness τ_a, the aerosol model, the surface albedo (including land and sea), and the solar zenith angle θ_0. Unless stated otherwise, the results are for RT calculations performed with the AAOT aerosol model and a water surface and with the Ispra aerosol model and the Po Valley typical albedo.

3.1.1 Instantaneous aerosol direct radiative effect

The instantaneous radiative effect at the surface, δF^{SRF} and at the top-of-atmosphere, δF^{TOA}, computed for every solar zenith angle θ_0 and every bin of the aerosol models (dependent on τ_a), are presented on Fig. 6. For the sake of clarity, only a subset of the θ_0 values is displayed (thus the angle for which the radiative effect is maximum, noted θ_0^{max}, might not be represented). The results for the case of the Po Valley
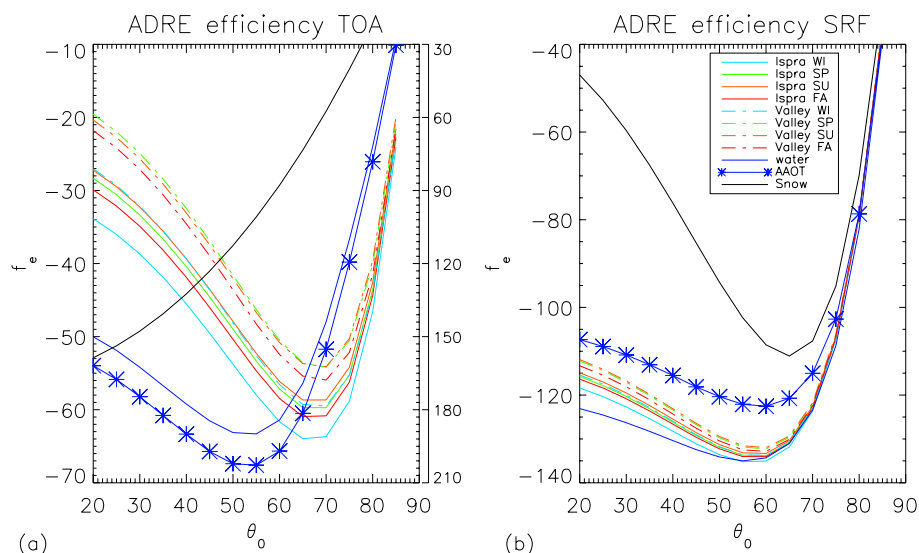
Fig. 7. Aerosol direct radiative effect efficiencies at TOA **(a)** and surface **(b)**. The blue line represents f_e computed over a water surface with the Ispra aerosol model. The blue line with asterisks is the AAOT reference case (AAOT aerosols and water surface). The other curves correspond to the Ispra aerosol model with typical albedos around Ispra and for the whole Po Valley (dashed lines) for the four seasons.

are shown for winter and summer albedos. At the surface, the dependence of δF^{SRF} on τ_a is close to linearity except for high solar zenith angles, whereas at TOA, this relationship departs from linearity for moderate τ_a. The curves for θ_0 equal to 80° should be viewed with caution considering the plane-parallel assumptions of the RT calculations.

The relationship between δF^{SRF} and θ_0 is very similar for the different terrestrial albedos and comparable for the water surface, even though the amplitude for a given τ_a is lower in that case (Fig. 6d–f). For the reference $\tau_a(500)$ (approximately 0.21) and for θ_0 below 65°, δF^{SRF} is close to $-26\,\mathrm{W\,m^{-2}}$ for the marine case and $-28\,\mathrm{W\,m^{-2}}$ for the Po Valley for the four seasons. For the bin of highest $\tau_a(500)$ (0.97), the maximum value of δF^{SRF} for the Po Valley is between -121 and $-119\,\mathrm{W\,m^{-2}}$ for the four seasons, whereas it is $-93\,\mathrm{W\,m^{-2}}$ for the marine case (for $\tau_a(500)$ equal to 0.89).

Conversely, the relationship between δF^{TOA} and θ_0 shows variations of amplitudes between seasons for the terrestrial case and a different angular dependence for the marine case. For instance for the reference $\tau_a(500)$ and θ_0 of 20°, δF^{TOA} is between -5.8 and $-7.5\,\mathrm{W\,m^{-2}}$ for terrestrial surfaces over the four seasons, and $-13.2\,\mathrm{W\,m^{-2}}$ for the marine case (a factor of two higher). For θ_0 equal to 60°, these numbers are from -13.6 to $-14.9\,\mathrm{W\,m^{-2}}$ and $-16.3\,\mathrm{W\,m^{-2}}$, respectively.

3.1.2 Aerosol direct radiative effect efficiencies

The instantaneous radiative efficiencies at TOA and surface are derived as the slope of the linear regression between δF and $\tau_a(500)$. Considering the non linearities noticed on Fig. 6

for high aerosol loads, the range of $\tau_a(500)$ values used for the regression is restricted to the first 13 bins, i.e., for $\tau_a(500)$ approximately lower than 0.5, that is the average value multiplied by the geometric standard deviation (see Table 1). The efficiencies computed on this interval are higher than those obtained over the whole range of τ_a but they are more representative of the actual τ_a variations. Figure 7 shows the radiative efficiencies at TOA and surface as a function of θ_0 for the various cases simulated: terrestrial surfaces with albedos representative of the Ispra area and the whole Po Valley (four seasons) and the Ispra aerosol model, and water cases with both AAOT and Ispra aerosol models and a very reflective surface (snow) with the Ispra aerosol model.

As documented in previous studies (e.g., Nemesure et al., 1995; Boucher, 1998b), the dependence on the solar zenith angle of the ADRE at the top of atmosphere (Fig. 7a) displays a well marked (negative) maximum at intermediate solar zenith angles. δF^{TOA} is lower at low θ_0, as the relative contribution of the aerosols in absorbing surface-reflected radiation (thus decreasing the overall efficiency of the atmosphere-surface system in reflecting the solar radiation) is larger. As anticipated in the previous section, the dependence of the ADRE at TOA is clearly affected by the characteristics of the surface. For θ_0 below 60°, f_e^{TOA} for the marine cases is higher (more negative) than for terrestrial surfaces, illustrating the main dependence of the ADRE with respect to surface albedo (e.g., Charlson et al., 1992; Haywood and Shine, 1995). This is particularly the case at low solar zenith angle. At 20°, f_e^{TOA} is equal to $-54\,\mathrm{W\,m^{-2}}\,\tau_a^{-1}$ over water with the AAOT aerosol model. The maximum f_e^{TOA} is found at 55° ($-68\,\mathrm{W\,m^{-2}}\,\tau_a^{-1}$ for the AAOT aerosol case), angle lower than that documented by Boucher and Tanré (2000),
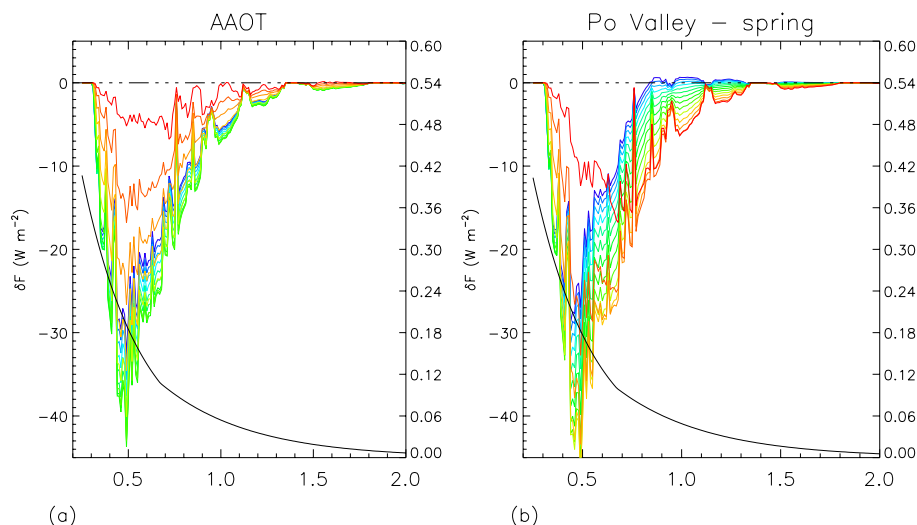
Fig. 8. Spectral dependency of δF^{TOA} obtained for the reference τ_a bin for increasing values of the solar zenith angle ranging from 20° (blue) to 85° (red), for the cases of the AAOT site **(a)** and the Po Valley in spring **(b)**. The reference τ_a is shown by the black line.

a shift that might be due to the aerosol types and a different treatment of the bidirectional reflectance of the water surface. A more absorbing aerosol, like that associated with Ispra, decreases f_e^{TOA} by approximately 4 W m^{-2} τ_a^{-1}. For solar zenith angles higher than 60°, f_e^{TOA} decreases sharply, as the water surface reflectivity rises according to the Fresnel law. Over the Po Valley, f_e^{TOA} is lowest at 20°, especially for the more reflecting case, in spring and summer, with -20 W m^{-2} τ_a^{-1} (a factor of almost 3 with respect to the equivalent marine case). The maximum efficiency is observed for $\theta_0^{\max}$ of 65–70° and ranges from -54 to -59 W m^{-2} τ_a^{-1} from winter to summer surface albedos. These values increase (more negative) for a less reflecting surface, like that found around Ispra. Over a very bright surface (snow), f_e^{TOA} becomes positive, with a maximum at low θ_0 (+150 W m^{-2} τ_a^{-1} at 20°). These values are in line with the findings in Ricchiazzi et al. (2005) for a continental aerosol type (+18 W m^{-2} for $\tau_a(550)$=0.1 at the same θ_0).

At the surface (Fig. 7b), the efficiencies f_e^{SRF} appear rather constant for θ_0 up to 60°, for all cases but the snow albedo, and all values are found in the range -107 to -135 W m^{-2} τ_a^{-1}, for θ_0 lower than 70°. For higher angles, the f_e^{SRF} curves converge towards smaller radiative effects. For all simulations, f_e^{SRF} is maximum (negative) for $\theta_0^{\max}$ between 55° and 60°. The location of this maximum depends only slightly on the surface reflectivity or aerosol model. For the marine case, the maximum f_e^{SRF} amounts to -123 and -135 W m^{-2} τ_a^{-1} for the AAOT and Ispra aerosol models, respectively, and it ranges from -132 to -134 W m^{-2} τ_a^{-1} for the Po Valley with different seasonal albedos. Two factors appear important in determining the amplitude of the surface ADRE for a given τ_a. The radiative efficiency at the surface decreases (less negative) for more reflecting surfaces which

is particulary visible for the snow case, showing a minimum of -45 W m^{-2} τ_a^{-1} at 20°. It increases for more absorbing aerosols, for instance by approximately 15% (for θ_0 up to 60°) if the AAOT aerosol model is substituted by the Ispra model used over a marine surface.

Similarly, the radiative efficiencies can be computed for a day by combining the instantaneous contributions for each sun zenith angle with the actual solar illumination cycle during the day. As for the linear regression performed on instantaneous values, only the first 13 τ_a bins are considered. Table 2 presents the radiative efficiencies f_e for both sites, computed for the 21st of every month. Logically, f_e values are identical at the two equinoxes for the AAOT site (this is not so for the Po Valley because of the seasonal cycle of the surface albedo). At AAOT from December to June, f_e^{TOA} ranges from -15 to -32 W m^{-2} τ_a^{-1} and f_e^{SRF} from -35 to -65 W m^{-2} τ_a^{-1}. For the Po Valley, f_e^{SRF} exhibits a larger seasonal variability from winter to summer (from -33 to -72 W m^{-2} τ_a^{-1}) while, interestingly, the annual variations of f_e^{TOA} are lower, between -17 and -24 W m^{-2} τ_a^{-1}. In fact at TOA, the longer duration of the day in summer, which increases the daily ADRE, is balanced over land by the much reduced effectiveness around noon (low θ_0, see Fig. 7a and Fig. 9 in Sect. 3.1.4).

Other estimates of the aerosol direct radiative effect are listed in Table 3 for regions mostly or partly influenced by continental/anthropogenic aerosols (these examples do not include situations with mostly dust or marine aerosols). Importantly, part of the variability of efficiency values given in Table 3 is due to differences in modelling and experimental approaches (including the spectral interval considered), in surface characteristics, in latitude, or in temporal scales. Notwithstanding this diversity, a comparison with this study
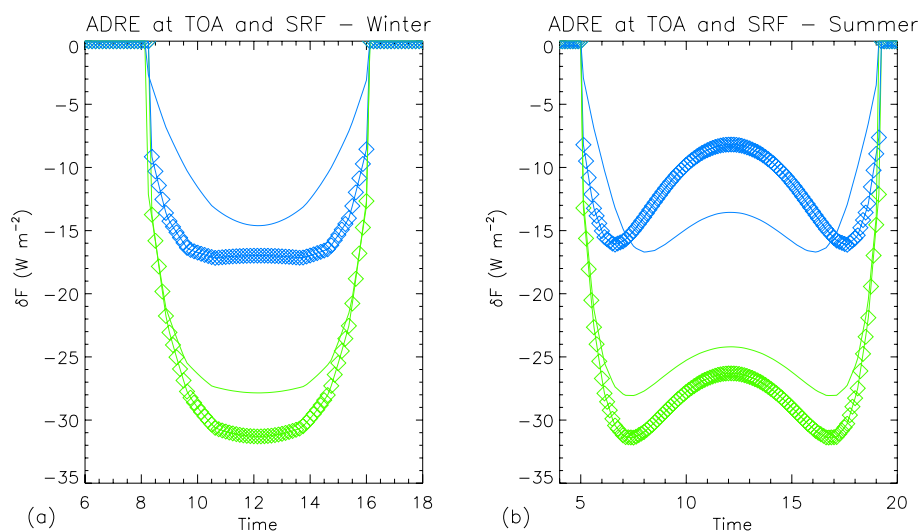
Fig. 9. Diurnal cycle of the aerosol direct radiative effect, computed for the reference bin ($\tau_a \simeq 0.21$) for 15 January **(a)** and July **(b)**. δF^{TOA} (blue) and δF^{SRF} (green) are represented for the Po Valley (line+diamonds) and the AAOT (line) cases.

Table 2. Daily aerosol direct radiative effect efficiencies at TOA and surface, for the 21st of every month, for the AAOT site and the Po Valley case. Units are $\mathrm{W\,m^{-2}\,\tau_a(500)^{-1}}$.

	AAOT		Po Valley	
Month	f_e^{TOA}	f_e^{SRF}	f_e^{TOA}	f_e^{SRF}
January	-17.2	-38.6	-19.5	-38.8
February	-22.6	-46.5	-23.0	-49.3
March	-26.7	-53.1	-22.3	-57.5
April	-29.7	-59.1	-23.1	-64.8
May	-31.7	-63.6	-23.7	-69.9
June	-32.5	-65.4	-24.4	-72.0
July	-31.7	-63.6	-24.0	-69.9
August	-29.6	-59.0	-23.3	-64.6
September	-26.7	-53.1	-23.2	-57.7
October	-22.3	-46.1	-21.4	-48.5
November	-16.9	-38.3	-18.2	-38.1
December	-14.8	-34.8	-17.3	-33.4

places the present estimates of ADRE in relation to aerosols and their radiative impacts in other regions. The radiative efficiencies documented in this work appear in the middle of the interval represented in Table 3 and are actually similar to various situations. For instance, both f_e^{TOA} and f_e^{SRF} for the Po Valley compare remarkably well with estimates given for the region of Vienna (Austria) in summer. Interestingly, they are also similar to the values documented for Kanpur (India). The radiative efficiencies obtained for the AAOT site can be favorably compared to other estimates given for northeastern Greece, the marine regions around Korea and Japan, or southwest of India in (boreal) winter-spring. The ratio of daily f_e at surface and TOA varies for the Po Valley case from 1.9 (December) to 3.0 (June) with an annual average

of 2.5. It varies in the interval 2.0 to 2.4 for the AAOT case (annual mean of 2.1). The present results are also consistent with the multi-site analysis of Zhou et al. (2005). These calculations and the comparisons with other ADRE estimates confirm a situation of moderately absorbing aerosols, coherent with the single scattering albedos characterizing the area.

3.1.3 Spectral dependence of the aerosol direct radiative effect

As discussed above, the effect of the surface reflectivity in determining the radiative effect is particularly marked at the top of atmosphere (Fig. 7), and can be further described in terms of its spectral distribution (Fig. 8, example given for the reference τ_a at the two sites). Obviously, for a given θ_0, the spectral distribution of the radiative effect is a combination of the solar irradiance spectrum and the spectral characteristics of the surface albedo and aerosol optical thickness.

As seen on Fig. 7a, the radiative effect for the AAOT case increases slightly from $20°$ to $50°$ and then decreases clearly for θ_0 beyond $60°$. This reduction is due to an increase of the surface reflectivity with θ_0 and appears to be uniformly distributed on the δF^{TOA} spectrum (see Fig. 8a, orange to red curves). For the Po Valley the initial increase of δF is steeper and decreases only at high solar zenith angles. As expected for aerosols of continental type, the radiative effect for wavelengths larger than $1\,\mu\mathrm{m}$ becomes negligible. Actually, most of the radiative energy changes are distributed in the spectral interval 0.4–$0.8\,\mu\mathrm{m}$. For the Po Valley, the marked increase in albedo from 0.5 to $0.9\,\mu\mathrm{m}$ results in a decrease of the negative radiative effect, that becomes even positive for small θ_0 values in the spectral range 0.75 to $1.3\,\mu\mathrm{m}$. Except at very high solar zenith angles, the largest radiative impact is for wavelengths around $0.5\,\mu\mathrm{m}$ (corresponding to the maximum of solar irradiance).

Table 3. Daily aerosol direct radiative efficiencies. The fourth column (λ) indicates the spectral domain considered (SW: shortwave broadband). The fifth column gives the observed τ_a and the associated wavelength, also used for the normalization of ADRE. All wavelengths are in μm. Units for f_e are $W\,m^{-2}\,\tau_a^{-1}$.

Area	Surface	Period	λ	τ_a	f_e^{TOA}	f_e^{SRF}
Lindenberg [1]	land	July–August	0.2–4	0.08–0.25 (0.55)	−48	−67
Almería [2]	land	June	0.44–0.78	0.41 (0.52)	−11	−57
Vienna [2]	land		0.44–0.78	0.39 (0.52)	−24	−68
Marseilles [3]	land	June–July	0.3–3	0.23–0.45 (0.5)	∼−24	−107
NE Greece [4]	sea	Aug	0.28–4	0.39 (0.5)	−21/−18	−55/−63
NE Greece [4]	sea/land	August	0.28–4	0.39 (0.5)	−12/−8	−49/−56
Crete [5]	sea/land	July–August	SW	0.1–0.5 (0.5)	−31	−85
Sede Boker [6]	land	year	0.17–2.27	(0.55)	−32/−12	−68/−56
Lampedusa [7]	sea/land	May	0.4–0.7	0.164 (0.53)	−4	−122
US E. Coast [8]	sea	July	SW	(0.55)	−30	−87
US E. Coast [9]	sea	July	SW	(VIS)	−53/−44	−96/−68
East. US [10]	land	June–July	SW	(SW)	−20	
US [11]	land	spr.-sum.	SW	(SW)	−33/−23	
N. America [12]	land	year	SW	(SW)	∼−25	
Gosan [13]	sea/land	April	SW	(0.5)		−73
Sea of Japan [14]	sea	April	SW	0.43±0.25 (0.5)	−27	−60
Gosan [15]	sea/land	November	SW	0.12–0.28 (0.5)		−79
NE Asia [16]	sea	Apr	0.3–4	(0.5)	−29/−18	−69/−90
Kaashidhoo [17]	sea	January–March	SW	0.1–0.7 (0.5)	−25	−73
Bay of Bengal [18]	sea	October	SW	0.43 (0.5)	−33	−59
SW India [19]	sea	March–April	0.25–4	0.44±0.13	−29/−22	−59/−72
Bangalore [20]	land	October–December	SW	0.24 (0.5)	+21	−97
Kanpur [21]	land	December–January	0.25–4	(0.5)	−25	−72

References and notes: [1] Wendling et al. (2002): Lindenberg (Germany), 80 km SE Berlin; [2] Horvath et al. (2002): Almería (coastal Spain), and Vienna (Austria); calculations are with respect to a background aerosol load; [3] Roger et al. (2006): Marseilles (SE France), albedo from MODIS; [4] Formenti et al. (2002): 2 values for 2 aerosol models; [5] Markowicz et al. (2002): includes cases of forest fire aerosols; [6] Derimian et al. (2006): annual average of $\tau_a(500)=0.20\pm0.11$; the radiative effect applies to the downwelling fluxes and is computed for the contribution of pollution aerosols only; maximum f_e^{TOA} ($-32\,W\,m^{-2}\,\tau_a(550)^{-1}$) is found in February–March, minimum (-12) in May–June, maximum f_e^{SRF} ($-68\,W\,m^{-2}\,\tau_a(550)^{-1}$) is found in March, minimum (-56) in November; [7] Meloni et al. (2003): computed for the case of 27 May 1999 (day with aerosol of northern origin, with highest Ångström exponent, 1.36), with $\tau_a(532)$ from Di Iorio et al. (2003); [8]: Hignett et al. (1999): US East Coast (TARFOX campaign); [9]: Russel et al. (1999): US East Coast (TARFOX campaign) with TARFOX aerosol models and τ_a averaged in the interval 0.3–0.7 μm (VIS); [10] Im et al. (2001): North Carolina (US), calculations with a box model; [11] Sheridan and Ogren (1999): central and eastern US, calculations with a box model; [12] Delene et al. (2002): central US, Alaska, Nova Scotia (Canada), calculations with a box model; [13] Bush and Valero (2003): Gosan, Island of Jeju (S Korea), ACE-Asia; [14] Markowicz et al. (2003): ACE-Asia; [15] Kim et al. (2005a): Gosan, Island of Jeju (S Korea), pollution event; [16] Kim et al. (2005b): measurements at Anmyon and Gosan (S Korea), and Amami-Oshima Island (Japan), only the non-dust cases are used here; [17] Satheesh and Ramanathan (2000): Kaashidhoo Island, SW of India; [18] Sumanth et al. (2004): coastal Bay of Bengal; [19] Moorthy et al. (2005): coastal SW India; [20] Babu et al. (2002) Bangalore (India); [21] Dey and Tripathi (2007): Kanpur (N India).

3.1.4 Diurnal cycle of the aerosol direct radiative effect

The diurnal cycle of δF^{TOA} and δF^{SRF} is derived by combining the radiative effect, computed for every solar zenith angle, with the θ_0 variations during 15 January (winter) and 15 July (summer). At this stage, the aerosol optical thickness is fixed at its reference value. In winter, at the latitude of both sites, θ_0 remains close to or larger than $\theta_0^{\max}$ and the maximum δF^{TOA} and δF^{SRF} are reached during the central part of the day (Fig. 9a). In summer δF^{SRF} is maximum around 07:00 a.m. and 05:00 p.m. and exhibits a visible reduction during the central part of the day (Fig. 9b). At TOA the same effect is visible, with maxima slightly shifted in time, due to a different dependence of the ADRE on θ_0 (Fig. 7). The daily cycle of δF^{TOA} is especially evident for the Po Valley, with a

maximum of about $-16\,W\,m^{-2}$ early in the morning and late in the afternoon, which is about twice as much as the value at noon. These results are associated with a decrease of the hemispheric upscatter fraction and have been documented in the context of other measurement series (e.g., Russel et al., 1999; Formenti et al., 2002; Wendling et al., 2002).

3.2 Sensitivity analysis

Sensitivity tests are here performed to assess the uncertainty of the ADRE estimates. The main sources of uncertainty in the radiative effect estimation are linked to the optical properties of the aerosols and their vertical distribution, in the sea/land surface reflectivity parametrization and in some approximations introduced at different steps of the calculation.
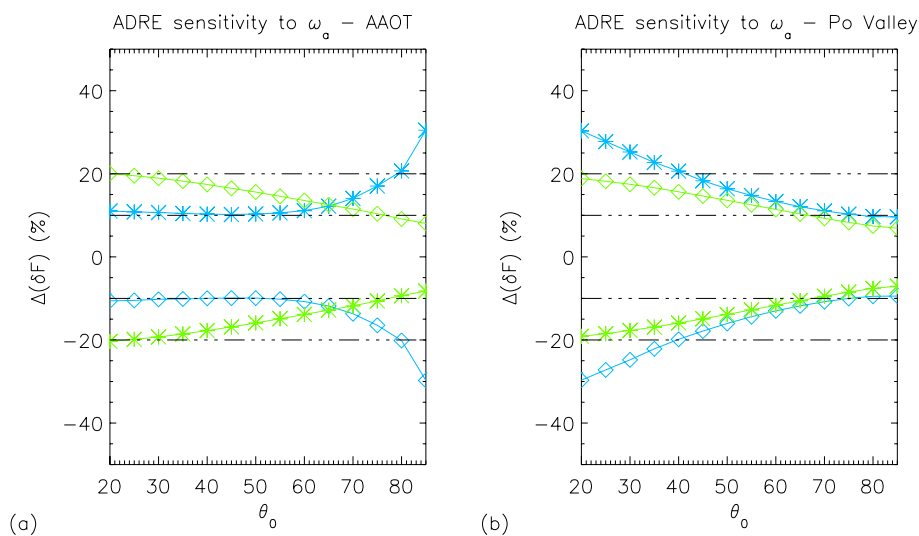
Fig. 10. Percentage variation of δF^{TOA} (blue) and δF^{SRF} (green) for $\omega_a = \omega_a + \delta \omega_a$ (asterisks) and $\omega_a = \omega_a - \delta \omega_a$ (diamonds), for the AAOT and Po Valley reference cases.

The effect of these sources is discussed and quantified below, to be used for an overall uncertainty budget.

3.2.1 Aerosol optical thickness

The expected accuracy of the aerosol optical thickness at 500 nm is 0.015 (Eck et al., 1999). This uncertainty has a different impact for low and high aerosol loads, resulting, e.g, in a relative error of more than 40% for the first bin (low τ_a) and around 2% for the last bin of the aerosol models, while it amounts to approximately 7% for the average values. In the uncertainty budget, the relationship between τ_a and δF is assumed linear, so that the related uncertainty on the radiative effect, Δ_τ, is equal to first order to the ratio $\delta \tau_a / \tau_a$. Part of this uncertainty is due to calibration and might result in a bias during a deployment period, whereas assumptions on the atmospheric conditions (e.g., pressure, ozone) lead to a variable error term (Eck et al., 1999).

3.2.2 Single scattering albedo

In the RT simulations, the single scattering albedo ω_a is assumed as a constant spectrum (see Sect. 2.2). For a sensitivity analysis, the uncertainty on ω_a, σ_ω, is estimated as the maximum of the dispersion around the mean value (standard deviation reported in Table 1) and 0.03, which is the uncertainty associated with the inversion process (Dubovik et al., 2000). Admittedly, there is an additional, unknown, uncertainty due to the absence of ω_a values associated with conditions of low aerosol loads. As for ω_a, the uncertainty term σ_ω is extrapolated to all wavelengths in the range 0.25 to $2.0\,\mu$m. Then, the radiative effect associated with aerosols having single scattering albedo equal to $\omega_a(\lambda) \pm \sigma_\omega(\lambda)$ has been computed for representative τ_a bins and the conditions associated with AAOT and the Po Valley, assuming a season-

ally averaged spectral surface albedo for the latter. The relative differences, with respect to the ADRE computed with the average ω_a, are represented on Fig. 10, for the reference τ_a bin. It is underlined here that all δF at TOA and surface observed in the present study are negative, snow cases excepted, and a positive relative difference (in%) means a reinforced negative effect.

For the AAOT site and the reference $\tau_a(500)$ (0.219), δF^{TOA} increases (more negative) for the more scattering aerosol (case $\omega_a + \sigma_\omega$), within 15% for θ_0 below 70° and by up to 20–30% for high θ_0 (see Fig. 10a). On the other hand, at the surface this less absorbing aerosol results in a radiative effect that is reduced by -20% to -8% for θ_0 from 20° to 85°. The effect of a more absorbing aerosol (case $\omega_a - \sigma_\omega$) gives specular results both at TOA and surface. These relative differences are little affected by the aerosol load: with τ_a as high as 0.6, the relative differences do not change by more than 3–4%, except for δF^{TOA} at θ_0 of 85° (8%). For the Po Valley case and the reference $\tau_a(500)$ (0.211) (Fig. 10b) the relative change in δF^{TOA} due to a change in ω_a is maximum for low θ_0 (30% at 20°) and decreases to ± 10% for high θ_0. A significant impact of τ_a is noticed for δF^{TOA}, particularly at low solar zenith angles: the relative differences for θ_0 equal to 20° is in the interval 25–35% but may reach 45% for high τ_a (0.65). The trend for δF^{SRF} is very similar to that described for AAOT, from 19% to 7% as θ_0 increases. As τ_a is varied, the relative differences for δF^{SRF} change by approximately 2%.

In the following, the reference $\tau_a(500)$ serves to define a typical uncertainty term due to ω_a. The relative sensitivity of δF with respect to the uncertainty on ω_a depends clearly on θ_0, both in magnitude and variations (including between sites), and this dependence is kept in the following error treatment.

3.2.3 Scattering phase function

In the aerosol models defined in Sect. 2.2, and unlike the assumption of a fixed ω_a spectrum, the evolution of the aerosol scattering phase function ψ_a with the aerosol load, expressed by the τ_a bin (Fig. 4), is taken into account in the set of RT calculations. The uncertainties of the ADRE associated with the uncertainties on ψ_a are assessed by considering the variations of ψ_a in an aerosol model bin. First, the logarithmic distance between each ψ_a (taken at 670 nm) included in the bin and the bin-averaged function is evaluated, and the curves are sorted accordingly (the distance is computed as the root mean square difference between log-transformed values of ψ_a over the available scattering angles). Then two sets of ψ_a are selected, each containing 10% of the bin population, and centered around the 16 and 84 percentiles of the distance distribution (i.e., at±one standard deviation of the average ψ_a). The respective averages of these two sets, noted $\psi_{a,1}$ and $\psi_{a,2}$ (see Fig. 11 for the AAOT case) are considered representative of the phase function dispersion and provide an estimate of the associated uncertainty. Interestingly, $\psi_{a,1}$ exhibits reduced forward and backward scattering peaks, and an increased scattering for scattering angles in the range 10 to 70°, and is associated with high τ_a values in the bin; $\psi_{a,2}$ shows an opposite behavior. Numerically, large differences are noticed in the very first angles of scattering, but this variation of the forward scattering peak does not have a large impact on the aerosol radiative effect.

Calculations have been performed with $\psi_{a,1}$ and $\psi_{a,2}$ for the AAOT and terrestrial conditions and for various bins, and the relative difference, noted Δ_ψ, with respect to the standard results is computed. In practice, Δ_ψ varies with the phase function used, the type of surface, τ_a and θ_0 in a rather complex way. For the sake of quantifying the related uncertainty term, the average relative effect during a day is computed for the central day of every season by considering the θ_0 variations; this appears confined within 4% (2%) for the Po Valley (AAOT) case at TOA and 1.5% at surface for both cases. These upper boundaries are conservatively chosen as estimate of Δ_ψ. These low values are explained by the fact that the aerosol type encountered in the region is fairly stable; the introduction of ψ_a representative of very different aerosol types is likely to have a much larger impact.

3.2.4 Influence of the aerosol vertical distribution

The diversity characterizing the vertical distribution of aerosols have been amply documented in various locations (e.g., Hartley et al., 2000; Redemann et al., 2003; Matthias et al., 2004). To assess the impact of this variability on the aerosol radiative effect, RT calculations have been conducted with three exponential vertical distributions, defined so that the amount of particles reaches 90% of the total at heights of 1, 2 and 3 km, and are compared with the results of the reference distribution (uniform up to 3 km). For these sim-
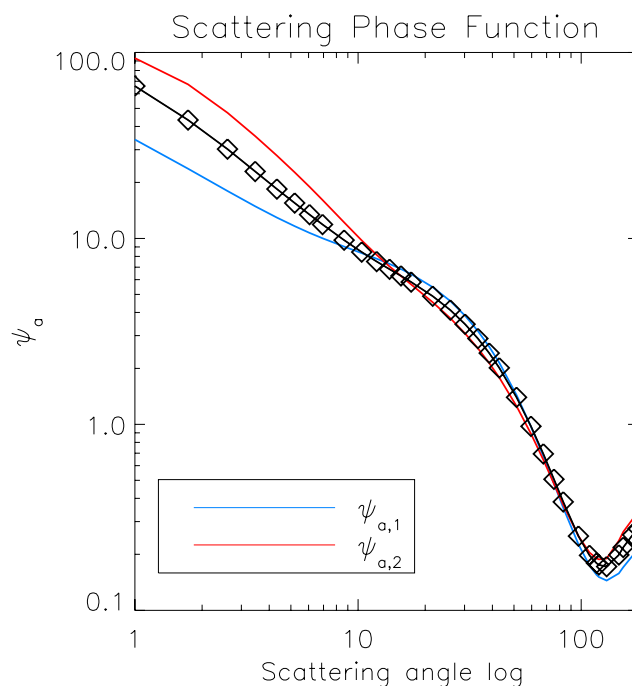

Fig. 11. Definition of the range of variation of ψ_a for the central τ_a bin, at the AAOT site.

ulations, the vertical resolution is refined to 250 m in the lower 3 km. The inherent optical properties of the aerosols are still maintained constant. Even though such tests are far from representing the full diversity of the observed aerosol layering, an exponential function has been used as a convenient way of depicting its main features for typical continental aerosols, including at European sites (e.g., Mattis et al., 2004; De Tomasi et al., 2006). On the other hand, complex vertical layering has been found for particular events, such as long range transport of desert dust or forest fire aerosols (including over Europe, for instance see Ansmann et al., 2004; Mattis et al., 2003, respectively), that are not the focus of the present study.

The results of the simulations performed for the reference τ_a are represented on Fig. 12 as relative differences with respect to the reference case (aerosol uniform up to 3 km). As expected, the largest relative differences Δ_z in radiative effect occur at TOA when the aerosol particles are concentrated close to the surface (90% of the aerosol load within 1 km) and for the highest solar zenith angles (−3% and −6% for θ_0 of 75° and 80°, respectively). δF^{SRF} exhibits a moderate dependence on the vertical distribution, with relative differences mostly within 1% for θ_0 below 80°. The change in vertical structure usually has a larger effect for the terrestrial case, particularly for low θ_0, (+4.5% at TOA and −1.5% at the surface, i.e., a more and less negative radiative effect, respectively). The increases in Δ_z noticeable for very large θ_0 should be considered with caution because of the approximation of a plane-parallel atmosphere in the RT calculations. In any case, these higher values are related to situations of low
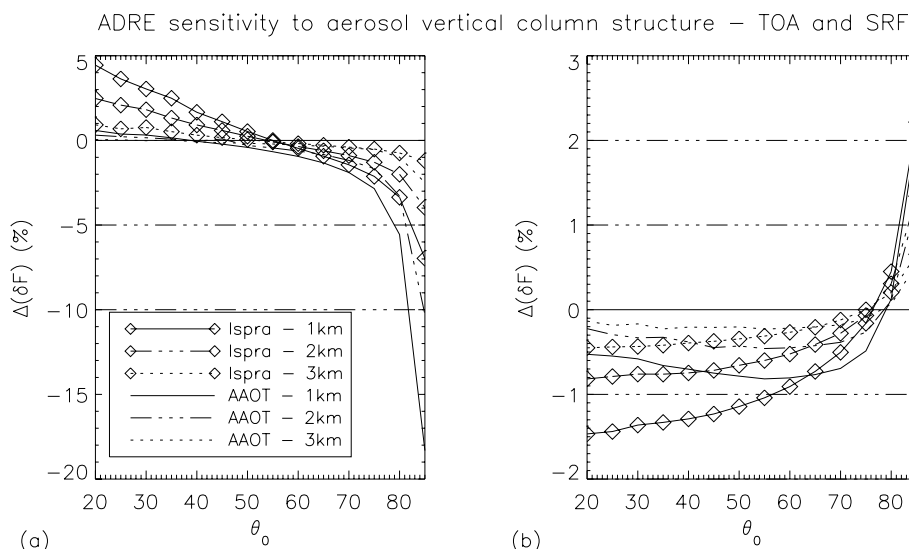
Fig. 12. Percentage variation of δF^{TOA} **(a)** and δF^{SRF} **(b)** for different aerosol vertical distributions. RT calculations with an exponential distribution with 90% of particles within 1 km, 2 km and 3 km are compared with the reference case (uniform distribution up to 3 km).

solar irradiance. Similar results are obtained for higher τ_a.

The estimate of the daily average effect of different vertical distributions is done by combining Δ_z of the 1-km exponential profile (worst case) with the θ_0 variation during the central day of each season. The result is within 3.4% at TOA and about 1% at the surface, and these values are used in the following uncertainty budget. Even though these results indicate a secondary effect of the aerosol vertical structure, it is stressed that they apply to the integrated effect (at TOA and surface). The vertical structure of the aerosol radiative effect, whose description is relevant for an accurate modelling of atmospheric dynamics, is obviously affected more strongly by the vertical distribution of the aerosols.

3.2.5 Influence of the surface albedo

The land surface albedo averaged over the region in proximity to the Ispra AERONET station exhibits values lower than the average for the whole Po Valley, for every season and for both black and white-sky albedos (Fig. 5). The spectral albedo, used as input to the RT model, is computed by weighting black and white sky albedos with the direct-to-diffuse irradiance ratio, which depends on θ_0 and τ_a. Consequently, the relative difference between the albedos ρ of the two regions also depends on θ_0 and τ_a, but in practice the related variations are small. Actually, for all conditions and seasons, relative differences between albedos associated with Ispra and the Po Valley (for ρ integrated between 0.25 and 2 μm) are found between 19% (in spring) and 22% (in winter).

As already seen on Fig. 7, δF is larger (more negative) in the case of an albedo representative of the region of Ispra than for the (higher) albedo averaged over the whole Po Valley. This is particularly visible for δF^{TOA} in conditions

of high values of τ_a and low solar zenith angles. The effect on ADRE at TOA, estimated along the central day of each season, is within 6% (winter) and 12% (spring), while, at the surface, it is much reduced, with differences not exceeding 2%.

Considering the geographical variability of the surface conditions encountered in the area of study (Fig. 1), the differences between the two sets of simulations appear appropriate to depict the sensitivity of δF to variations of ρ. Thus the relative uncertainty of δF due to the uncertainty on ρ, noted Δ_ρ, can be directly estimated by scaling the differences between the two sets of simulations with the absolute accuracy characterizing the MODIS product ($\pm$0.02, Sect. 2.3). The dependence of Δ_ρ on θ_0 is conserved in the estimates of the uncertainty budget for δF. Typically, the resulting uncertainties on the daily time scale are on average less than 1% for δF^{SRF} and vary between 3.6% and 6.8% from winter to summer for δF^{TOA}. Admittedly, these values do not foresee specific ground conditions such as heavy snow cover or flooded rice paddy fields that can be found in the western Valley.

For the marine conditions, RT calculations have been performed with different wind speeds, including 1 and 10 m s^{-1}. The resulting relative differences vary mostly with θ_0, $\sim$5–10% at the top of atmosphere and 1% at the surface. Conservatively, an uncertainty of 10% is assumed for δF^{TOA}. This appears consistent with the assumptions made by Yu et al. (2004).

3.2.6 Influence of the diurnal cycle

In all calculations so far, the aerosol optical thickness was taken constant during the day. This is justified for the sake of simplicity and the fact that time resolved daily series of τ_a are
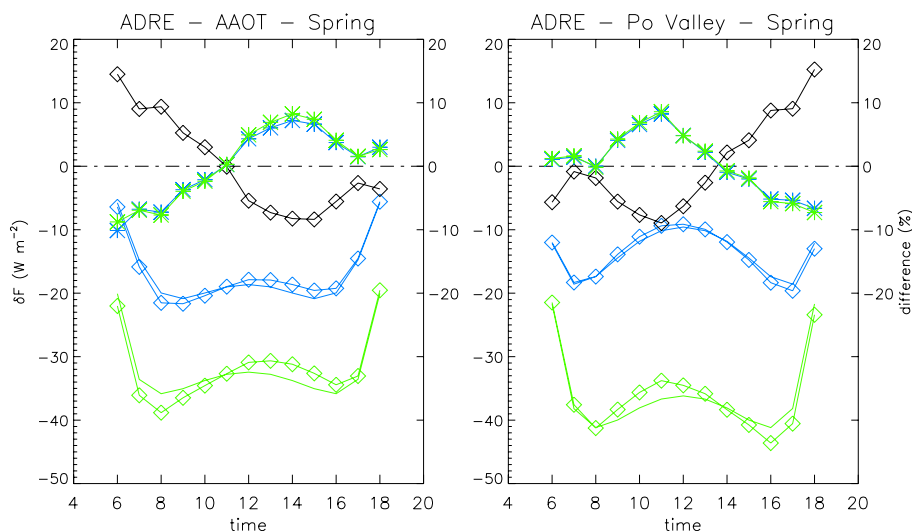
Fig. 13. Influence on the aerosol direct radiative effect of the diurnal cycle of τ_a. δF^{TOA} (blue) and δF^{SRF} (green) are computed for the two cases using constant daily values for τ_a (line), and a diurnally-resolved τ_a (line with diamonds). The δF scale is on the left-hand side. The associated relative differences of δF are shown by the corresponding colored lines with asterisks and the relative diurnal variability of τ_a is in black with diamonds (right-hand axis).

not always available for the determination of the aerosol radiative effect. However, τ_a values measured at both sites exhibit significant diurnal variations (Mélin and Zibordi, 2005). The related impact on the radiative effect is here assessed, for each season, by comparing δF computed for τ_a assumed constant along the day and varying according to the seasonally averaged diurnal cycle, computed as by Smirnov et al. (2002) (see Fig. 13 for the example of spring and the reference τ_a). The relative differences in radiative effect, Δ_d, mirror the τ_a variations along the day. Daily averages of δF are always within 0.8% for the AAOT site and aerosol model, due to compensation of morning and evening τ_a variations. This is not so in the case represented by Ispra, where τ_a around noon tends to be lower than the daily average. Consequently, Δ_d is higher, up to 1.9% and 2.1% in winter, for TOA and surface, respectively. Clearly, daily variations of τ_a much larger than the seasonal average might occur, but in general the use of a constant τ_a (equal to the daily average) for computing the daily integrated δF seems a safe approximation, favored by the quasi linearity of δF versus τ_a.

3.2.7 Overall uncertainty budget

The different sources of uncertainty described above and their impact on δF^{TOA} and δF^{SRF} are combined in order to derive an estimate of the uncertainty at daily and monthly scales (see Sect. 4.1 and Sect. 4.2). The various uncertainty terms described above and assumed independent are summed to estimate the uncertainty Δ_D for the daily aerosol radiative effect δF:

$$\Delta_D = (\Delta_\tau^2 + \Delta_\omega^2 + \Delta_\psi^2 + \Delta_z^2 + \Delta_\rho^2 + \Delta_d^2)^{1/2}. \qquad (1)$$

For the monthly ADRE averages, we distinguish between "random" errors, which can be minimized when considering repeated measurements on the same site, and "systematic" error contributions, that are not reduced by averaging. The uncertainties associated with the variations of aerosol optical properties (ω_a and ψ_a) in a bin are assumed variable, whereas the uncertainties associated with methodological assumptions (fixed homogeneous vertical distribution and constant τ_a during the day) and with the characteristics of the surface albedo are assumed systematic. Uncertainties on τ_a are partly due to uncertainties on environmental variables (pressure, ozone, ...) and calibration. The latter term might result in a systematic error during a deployment period. Conservatively, it is assumed to be dominant (see Eck et al., 1999, for a discussion) and thus systematic. Therefore, the error on the monthly average is computed as:

$$\Delta_M = (\Delta_\tau^2 + \frac{\Delta_\omega^2}{N_d} + \frac{\Delta_\psi^2}{N_d} + \Delta_z^2 + \Delta_\rho^2 + \Delta_d^2)^{1/2} \qquad (2)$$

where N_d is the number of days available in the month.

4 Estimates of the aerosol direct radiative effect

4.1 Daily statistics

The available AERONET time series described in Sect. 2.1 serve for the computation of the clear sky aerosol direct radiative effect along the entire time period. For regional studies, it is important to consider the whole frequency distribution of the aerosol load, and not only monthly or seasonal averages; these smooth out events that potentially have a strong
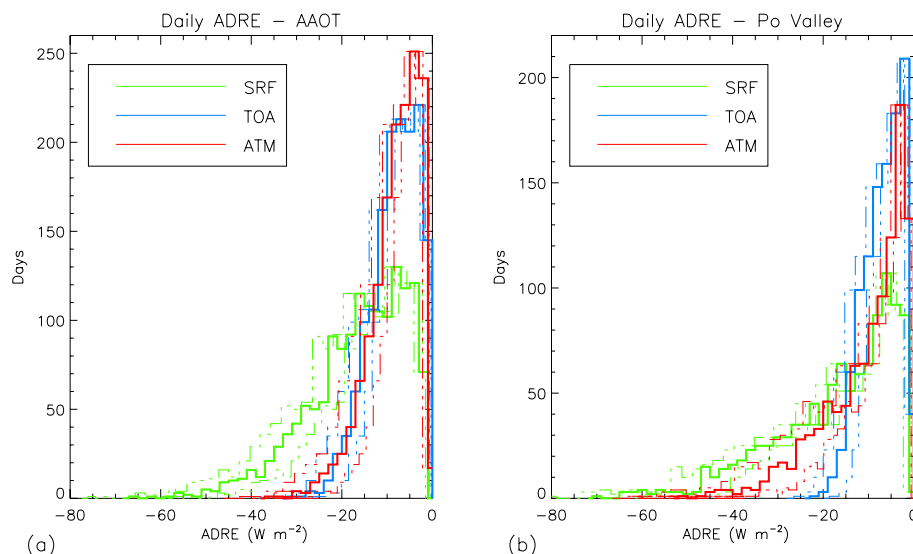
Fig. 14. Frequency distributions (in number of clear-sky days) of δF^{TOA} (blue), δF^{SRF} (green) and δF^{ATM} (red) occurrences, for the AAOT **(a)** and Po Valley **(b)** cases. The dashed lines bracketing each quantile of daily estimates represent the corresponding uncertainty. The arithmetic averages for the AAOT site of δF^{TOA}, δF^{SRF} and δF^{ATM} are -8.4, -16.6 and $+8.3\,\mathrm{W\,m^{-2}}$, respectively; for the Po Valley case, they are -6.7, -17.3 and $+10.6\,\mathrm{W\,m^{-2}}$ (see Sect. 4.1 for geometric means).

impact on the radiative budget (besides the statistics on air quality monitoring). Estimates of ADRE are performed for clear sky days with an associated value of $\tau_a(500)$. Here these are arbitrarily defined as the days with a minimum number of optical measurements during the day, proportional to the day length, from 12 in June to 6 in December. These thresholds affect the number of days classified as clear but not the main statistical features of the ADRE frequency distribution represented on Fig. 14. The dashed lines bracketing each quantile of daily estimates represent the corresponding uncertainty, computed as in Eq. 1 ($\delta F \pm \Delta_D \delta F$). The results presented for the terrestrial case are derived from the LUT constructed with the typical albedo for the Po Valley and the Ispra aerosols. As anticipated earlier, the aerosols at Ispra are here considered representative of the conditions in the western part of the Valley; considering the relative homogeneity of the surface conditions for the region of interest (Fig. 1), it seems more relevant for the present regional analysis to select the corresponding albedo. In any case, the ADRE for the actual site of Ispra differs only slightly. Finally, in line with the hypothesis of a log-normal distribution for τ_a, log-transformed statistics for δF are preferred to describe the frequency distributions (arithmetic means are given for completeness in the legend of Fig. 14).

At the AAOT site (1497 days classified as clear sky), δF^{SRF} amounts on average to $-13.0\,\mathrm{W\,m^{-2}}$ with extreme values up to $-60\,\mathrm{W\,m^{-2}}$ in summer. The δF^{TOA} distribution is centered around $-6.5\,\mathrm{W\,m^{-2}}$ and ranges up to $-30\,\mathrm{W\,m^{-2}}$. The ratio of surface and TOA ADRE is in the range 1.8 to 2.5 with average equal to 2.0. For conditions representative of the western Po Valley (1050 days classified

as clear sky), δF^{SRF} and δF^{TOA} are -12.2 and $-5.2\,\mathrm{W\,m^{-2}}$, with the highest values beyond $-70\,\mathrm{W\,m^{-2}}$ and $-20\,\mathrm{W\,m^{-2}}$, respectively. With respect to the AAOT site, the higher values at the surface are mainly due to the lower ω_a, while at TOA the effect is reduced due to the surface albedo. The ratio of δF^{SRF} and δF^{TOA} amounts on average to 2.4 and exhibits a large variability (1.6 to 3.7), which can be attributed to a larger variability in ω_a and the variations of the surface albedo during the year. If similar statistics are computed by season, the geometric averages for δF^{SRF} vary for both sites between approximately -6 and $-19\,\mathrm{W\,m^{-2}}$ from winter to summer. This evolution for δF^{TOA} is from -2.7 to $-9.9\,\mathrm{W\,m^{-2}}$ for AAOT, and -3.2 to $-7.1\,\mathrm{W\,m^{-2}}$ for the Po Valley case.

For the AAOT site, the average error terms for δF^{SRF} and δF^{TOA} are 18% (or $2.7\,\mathrm{W\,m^{-2}}$) and 20% (or $1.5\,\mathrm{W\,m^{-2}}$), respectively. The average error for δF^{SRF} for the Po Valley is 19% ($2.6\,\mathrm{W\,m^{-2}}$); the relative error for δF^{TOA} is 23% ($1.3\,\mathrm{W\,m^{-2}}$), a figure higher than at AAOT due to the higher sensitivity on ω_a. For both sites, the uncertainties on τ_a and ω_a contribute to most of the overall uncertainty for δF^{SRF} (approximately more than 90%) and in comparable proportions (even though varying with site and season). For δF^{TOA}, the other error terms take more importance, particularly the uncertainty due to the surface albedo. The latter is assumed as 10% for marine surfaces and is on average around 5% for land conditions (see Sect. 3.2.5).

The average atmospheric radiative effect δF^{ATM}, computed as $\delta F^{\mathrm{TOA}} - \delta F^{\mathrm{SRF}}$, is found slightly higher for the terrestrial conditions ($+6.8\,\mathrm{W\,m^{-2}}$) than at AAOT ($+6.5\,\mathrm{W\,m^{-2}}$), a difference mostly induced by a weaker

δF^{TOA} favored by a higher surface reflectivity. The long time series offer the unique opportunity to give an estimate of the spatial gradient in radiative effect due to aerosols at the scale of the Po Valley. As a simplification, the days classified as clear for both sites (673) are considered as the sample population to compute the gradient in atmospheric radiative effect (see Fig. 15 for the frequency distribution). These estimates are based only on differences between sites located at two ends of the Po Valley, but even though larger gradients might be observed locally in between, they provide an interesting insight into the spatial distribution of δF^{ATM} at a regional scale. The gradient is mostly positive towards Ispra (larger heating) with an overall average of $3.8\,\mathrm{W\,m^{-2}}$. Actually, δF^{ATM} appears larger in the Po Valley conditions in 65% of the cases. This is only partly explained by a larger τ_a (in 55% of the cases). Differences in ω_a and surface boundary conditions further modulate the atmospheric radiative gradient; in fact the daily radiative efficiency for the atmosphere, f_e^{ATM}, averaged over the same population, appears higher for the Po Valley conditions, $38\,\mathrm{W\,m^{-2}\,\tau_a^{-1}}$ versus $31\,\mathrm{W\,m^{-2}\,\tau_a^{-1}}$ for the AAOT site. The average of the absolute differences $|\delta F^{\mathrm{ATM}}(\text{Po Valley})-\delta F^{\mathrm{ATM}}(\text{AAOT})|$ is $6.3\,\mathrm{W\,m^{-2}}$ (or $2.1\,\mathrm{W\,m^{-2}}$ per $100\,\mathrm{km}$), and regularly exceed $10\,\mathrm{W\,m^{-2}}$ (in 23% of the cases).

4.2 Seasonal analysis

Subsequently, monthly averages of the aerosol radiative effect are derived from the daily series. Then, the average seasonal cycle is computed using the available years and is combined with the cloud fraction CF (provided by the International Satellite Cloud Climatology Project, Rossow and Schiffer, 1999) to yield the monthly climatology of the aerosol direct radiative effect. Figure 16 represents δF^{TOA}, δF^{SRF} and δF^{ATM}, together with a $\pm\sigma$ bar representing the inter-annual variations around the climatological average (also weighted by the clear-sky fraction). The aerosol optical depth at $500\,\mathrm{nm}$ and the clear-sky fraction are also displayed. At the AAOT site, δF^{SRF} increases from winter ($-1.7\,\mathrm{W\,m^{-2}}$ in December) to summer ($-12.9\,\mathrm{W\,m^{-2}}$ in August), a seasonal excursion reinforced by the correlated seasonal cycles of clear-sky fraction and sun illumination. The ADRE at the top-of-atmosphere exhibits the same seasonal behavior, ranging from -0.7 to $-6.6\,\mathrm{W\,m^{-2}}$ for the same months. Consequently, the atmospheric heating, coming from the difference of the terms above, presents again a minimum in December ($+1.0\,\mathrm{W\,m^{-2}}$) and a maximum in August ($+6.3\,\mathrm{W\,m^{-2}}$). The seasonal trend derived for the Po Valley region is similar, with δF^{SRF} increasing from winter ($-1.9\,\mathrm{W\,m^{-2}}$ in December) to summer ($-13.7\,\mathrm{W\,m^{-2}}$ in June), and similarly with δF^{TOA} increasing from $-1.0\,\mathrm{W\,m^{-2}}$ in December to $-4.8\,\mathrm{W\,m^{-2}}$ in July. The atmospheric heating is as high as $+9.1\,\mathrm{W\,m^{-2}}$ in June, and is minimum in December ($0.9\,\mathrm{W\,m^{-2}}$). For both cases, the error budget represented by Δ_M (Eq. 2) amounts to ap-
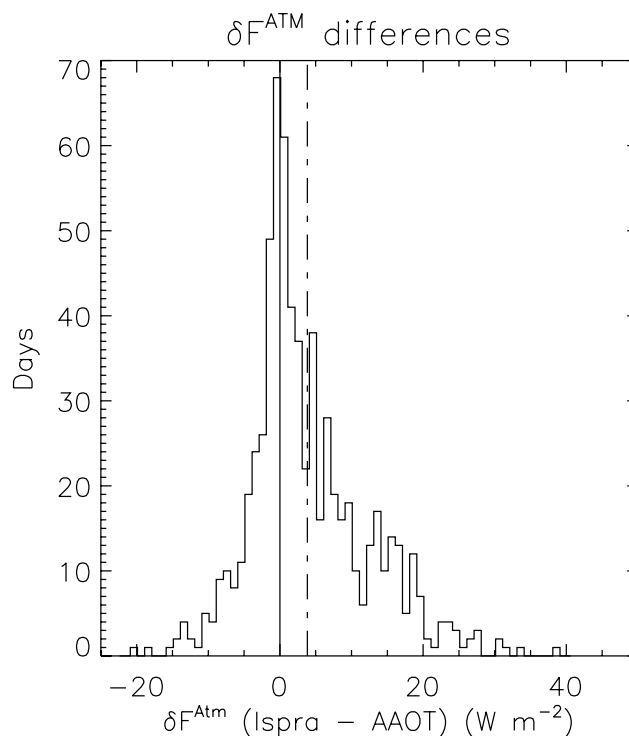

Fig. 15. Frequency distributions (in number of common clear-sky days) of the differences between the aerosol direct radiative effect for the atmosphere δF^{ATM} between the Po Valley and AAOT cases.

proximately 13% in winter and 3–5% in summer. The higher value of the monthly uncertainty term in winter is explained by a lower number of days during winter months and the lower average τ_a in that season, leading to higher relative uncertainties.

5 Conclusions

The direct radiative effect induced by aerosols is computed for the Po Valley region and the adjacent North Adriatic Sea, from long term time series of AERONET measurements and MODIS albedo data. For the sites of AAOT and Ispra, the overall averages for $\tau_a(500)$ and α are approximately 0.21 and 1.51, respectively. Besides the nature of the surface, the main difference between the two sites is a higher absorption for the Ispra aerosols, with an average $\omega_a(440)$ of 0.928 ± 0.032, as compared to AAOT's 0.956 ± 0.017.

The different surface reflectivity over land and sea concurs to significant differences in radiative efficiencies f_e at TOA (Fig. 7 and Table 2), varying for daily values along the year from -17 to $-24\,\mathrm{W\,m^{-2}\,\tau_a^{-1}}$ for the inner Po Valley conditions, and from -15 to $-32\,\mathrm{W\,m^{-2}\,\tau_a^{-1}}$ for the AAOT case. The efficiency at surface is more similar between sites in amplitude and temporal dependence, a convergence favored by a compensation between the effects of different ω_a and
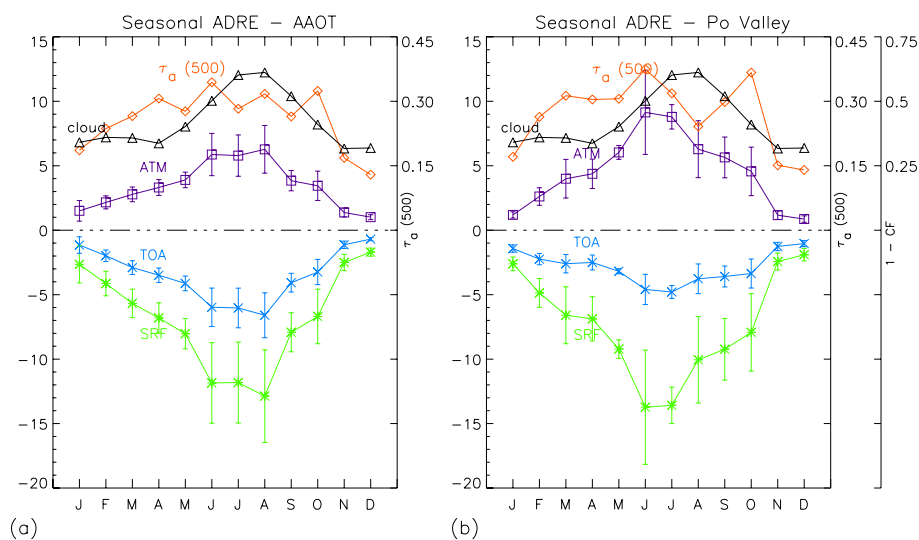
Fig. 16. Monthly average δF^{TOA} (blue), δF^{SRF} (green), δF^{ATM} (violet), τ_a (orange) and the clear-sky fraction (1-CF), for the AAOT **(a)** and Po Valley **(b)** cases. The left-hand axis is for the δF terms; specific axis are on the right-hand side for τ_a and the clear-sky fraction.

surface conditions (see Fig. 7). The variations from December to June for f_e^{SRF} are -33 to -72 W m^{-2} τ_a^{-1} for the Po Valley case and -35 to -65 W m^{-2} τ_a^{-1} for the AAOT site. In terms of daily radiative effect, the frequency distributions of δF^{TOA}, δF^{SRF} and δF^{ATM} have a geometric average of -5.2, -12.2 and $+6.8$ W m^{-2}, respectively, for the Po Valley case, and -6.5, -13.0 and $+6.5$ W m^{-2} for the marine site. On any given day, these radiative effects can be much higher (see Fig. 14). Furthermore, the large data set available gives the opportunity of analyzing a representative frequency distribution of the atmospheric heating spatial gradient between two ends of the Po Valley created by the aerosols in clear-sky conditions. This gradient is skewed towards a larger heating in the western part of the Valley and its average absolute value amounts to 6.3 W m^{-2}. Finally, a monthly climatology has been derived using seasonal values of the clear-sky fraction. For the Po Valley case, the climatological ADRE at TOA and surface peaks in summer at values of -4.8 and -13.7 W m^{-2}, respectively. The corresponding values for the AAOT site are -6.6 and -12.9 W m^{-2}. All these results point to a significant role of the aerosols in the radiative budget of the region.

An attempt has been made to accompany the estimates of the clear sky aerosol radiative effect in the region by a comprehensive uncertainty budget. The sources of uncertainty considered are mostly related to the measurements or determination of aerosol optical properties (τ_a, ω_a and ψ_a), the construction of the aerosol models (with properties either constant or varying dynamically with the aerosol load), assumptions on the aerosol vertical distribution, and the surface reflectivity. Not surprisingly, the uncertainties on τ_a and ω_a usually dominate the error budget, but secondary terms, like that associated with the surface conditions, are also sig-

nificant contributors particularly for the TOA effect. The uncertainty on the daily values has been estimated to be overall of the order of 20%. It is underlined that this uncertainty analysis is restricted to the framework of clear sky estimates. The global effect of aerosols on the region needs to include all interactions between aerosols and clouds but these complex and multi-faceted effects have not been considered in the present study. The integration of complementary measurements and chemical and transport modelling into a comprehensive monitoring system would be a logical avenue towards an improved assessment of the regional climate.

In any case, the emergence of a decade-long record of aerosol data obtained from optical measurements contributes to a better definition of the radiative budget of the Po Valley and adjacent marine area. This is relevant in the context of reduced emissions in western Europe (particularly for sulfate; Stern, 2006; Manktelow et al., 2007) and possible remote influences from inter-continental transport. In the case of the Po Valley (as in most of western Europe), an inversion in the temporal trend of solar radiation has been noticed in the 1980s (from "dimming" to "brightening", Norris and Wild, 2007), with the recent decrease likely related to a lower aerosol burden. As the time series of the field measurements lengthens, it further supports, in conjunction with other monitoring efforts, the analyzes of long term evolution of the aerosol load and associated radiative effect in this region characterized by high aerosol levels.

Edited by: K. Carslaw

References

Anderson, G. L., Clough, S. A., Kneizys, F. X., Chetwynd, J. H., and Shettle, E. P.: AFGL atmospheric concentration profiles (0–120 km), AFGL-TR86-0110, Air Force Geophys. Lab., Hanscom Air Force Base, MA, USA, 1986.

Ansmann, A., Bösenberg, J., Chaikovsky, A., Comerón, A., Eckhardt, S., Eixmann, R., Freudenthaler, V., Ginoux, P., Komguem, L., Linné, H., López Márquez, M. A., Matthias, V., Mattis, I., Mitev, V., Müller, D., Music, S., Nickovic, S., Pelon, J., Sauvage, L., Sobolewsky, P., Srivastava, M. K., Stohl, A., Torres, O., Vaughan, G., Wandinger, U., and Wiegner, M.: Long-range transport of Saharan dust to northern Europe: The 11–16 October 2001 outbreak observed with EARLINET, J. Geophys. Res., 108, 4783, doi:10.1029/2003JD003757, 2004.

Babu, S. S., Satheesh, S. K., and Moorthy, K. K.: Aerosol radiative forcing due to enhanced black carbon at an urban site in India, Geophys. Res. Lett., 29, 1880, doi:10.1029/2002GL015826, 2002.

Barnaba, F. and Gobbi, G. P.: Aerosol seasonal variability over the Mediterranean region and relative impact of maritime, continental and Saharan dust particles over the basin from MODIS data in the year 2001, Atmos. Chem. Phys., 4, 2367–2391, 2004, http://www.atmos-chem-phys.net/4/2367/2004/.

Beirle, S., Platt, U., Wenig, M., and Wagner, T.: Highly resolved global distribution of tropospheric NO$_2$ using GOME narrow swath mode data, Atmos. Chem. Phys., 4, 1913–1924, 2004, http://www.atmos-chem-phys.net/4/1913/2004/.

Bellouin, N., Boucher, O., Tanré, D., and Dubovic, O.: Aerosol absorption over the clear-sky oceans deduced from POLDER-1 and AERONET observations, Geophys. Res. Lett., 30, 1748, doi:10.10292003GL017121, 2003.

Boucher, O.: On aerosol direct shortwave forcing and the Henyey-Greenstein phase function, J. Atmos. Sci., 55, 128–134, 1998.

Boucher, O., Schwartz, S. E., Ackerman, T. P., Anderson, T. L., Bergstrom, B., Bonnel, B., Chýlek, P., Dahlback, A., Fouquart, Y., Fu, Q., Halthore, R. N., Haywood, J. M., Iversen, T., Kato, S., Kinne, S., Kirkevåg, A., Knapp, K. R., Lacis, A., Laszlo, I., Mishchenko, M. I., Nemesure, S., Ramaswamy, V., Roberts, D. L., Russell, P., Schlesinger, M. E., Stephens, G. L., Wagener, R., Wang, M., Wong, J., and Yang, F.: Intercomparison of models representing direct shortwave radiative forcing by sulfate aerosols, J. Geophys. Res., 103, 16 979–16 998, 1998.

Boucher, O. and Tanré, D.: Estimation of the aerosol perturbation to the Earth's radiative budget over oceans using POLDER satellite aerosol retrievals, Geophys. Res. Lett., 27, 1103–1106, 2000.

Bush, B. C. and Valero, F. P. J.: Surface aerosol radiative forcing at Gosan during the ACE-Asia campaign, J. Geophys. Res., 108, 8660, doi:10.1029/2002JD003233, 2003.

Charlson, R. J., Schwartz, S. E., Hales, J. M., Cess, R. D., Coakley, J. A., Hanses, J., and Hofmann, D. J.: Climate forcing by anthropogenic aerosols, Science, 255, 423–430, 1992.

Chazette, P., Randriamiarisoa, H., Sanak, J., Couvert, P., and Flamant, C.: Optical properties of urban aerosol from airborne and ground-based in situ measurements performed during the Etude et Simulation de la Qualité de l'air en Ile-de-France (ESQUIF) program, J. Geophys. Res., 110, D02206, doi:10.1029/2004JD004810, 2005.

Chu, D. A., Kaufman, Y. J., Zibordi, G., Chern, J. D., Mao, J., Li, C. and Holben, B. N.: Global monitoring of air pollution over land from the Earth Observing System – Terra Moderate Resolution Imaging Spectroradiometer (MODIS), J. Geophys. Res., 108, 4661, doi:10.1029/2002JD003179, 2003.

Chung, C. E., Ramanathan, V., and Kiehl, J. T.: Effects of the South Asian absorbing haze on the northeast monsoon and surface-air heat exchange, J. Climate, 15, 2462–2476, 2002.

Cox, C. and Munk, W.: Measurement of the roughness of the sea surface from photographs of the Sun's glitter, J. Opt. Soc. Am., 44(11), 838–850, 1956.

Delene, D. J. and Ogren, J. A.: Variability of aerosol optical properties at four North American surface monitoring sites, J. Atmos. Sci., 59, 1135–1150, 2002.

Derimian, Y., Karnieli, A., Kaufman, Y. J., Andreae, M. O., Andreae, T. W., Dubovik, O., Maenhaut, W., Koren, I., and Holben, B. N.: Dust and pollution aerosols over the Negev desert, Israel: Properties, transport and radiative effect, J. Geophys. Res., 111, D05205, doi:10.1029/2005JD006549, 2006.

De Tomasi, F., Tafuro, A. M., and Perrone, M. R.: Height and seasonal dependence of aerosol optical properties over southeast Italy, J. Geophys. Res., 111, D10203, doi:10.1029/2005GL006779, 2006.

Dey, S. and Tripathi, S. N.: Estimation of aerosol optical properties and radiative effects in the Ganga basin, northern India, during the wintertime, J. Geophys. Res., 112, D03203, doi:10.1029/2006JD007267, 2007.

Di Iorio, T., di Sarra, A., Junkermann, W., Cacciani, M., Fiocco, G., Fuà, D.: Tropospheric aerosols in the Mediterranean: 1. Microphysical and optical properties, J. Geophys. Res., 108, 4316, doi:10.1029/2002JD002815, 2003.

Dubovik, O. and King, M. D.: A flexible inversion algorithm for retrieval of aerosol optical properties from Sun and sky radiance measurements, J. Geophys. Res., 105, 20 673–20 696, 2000.

Dubovik, O., Smirnov, A., Holben, B. N., King, M. D., Kaufman, Y. J., Eck, T. F., and Slutsker, I.: Accuracy assessments of aerosol optical properties retrieved from AERONET Sun and sky radiance measurements, J. Geophys. Res., 105, 9791–9806, 2000.

Dubovik, O., Holben, B. N., Eck, T. F., Smirnov, A., Kaufman, Y. J., King, M. D., Tanré, D., and Slutsker, I.: Variability of ab-

sorption and optical properties of key aerosol types observed in worldwide locations, J. Atmos. Sci., 59, 590–608, 2002.

Eck, T. F., Holben, B. N., Reid, J. S., Dubovik, O., Smirnov, A., O'Neill, N. T., Slutsker, I., and Kinne, S.: The wavelength dependence of the optical depth of biomass burning, urban and desert dust aerosols, J. Geophys. Res., 104, 31 333–31 350, 1999.

Estellés, V., Martínez-Lozano, J. A., Utrillas, M. P., and Campanelli, M.: Columnar aerosol properties in Valencia (Spain) by ground-based Sun photometry, J. Geophys. Res., 112, D11201, doi:10.1029/2006JD008167, 2007.

Formenti, P., Boucher, O., Reiner, T., Sprung, D., Andreae, M. O., Wendisch, M., Wex, H., Kinred, D., Tzortziou, M., Varasas, A., and Zerefos, C.: STAAARTE-MED 1998 summer airborne measurements over the Aegean Sea. 2. Aerosol scattering and absorption and radiative calculations, J. Geophys. Res., 107, D21, 4551, doi:10.1029/2001JD001536, 2002.

Friedl, M. A., McIver, D. K., Hodges, J. C. F., Zhang, X. Y., Muchoney, D., Strahler, A. H., Woodcock, C. E., Gopal, S., Schneider, A., Cooper, A., Baccini, A., Gao, F., and Schaaf, C.: Global land cover mapping from MODIS: Algorithms and early results, Remote Sens. Environ., 83, 287–302, 2002.

Hansen, J. and Travis, L. D.: Light scattering in planetary atmospheres, Space Sci. Rev., 16, 527–610, 1974.

Hansen, J., Sato, M., and Ruedy, R.: Radiative forcing and climate response, J. Geophys. Res., 102, 6831–6864, 1997.

Hartley, W. S., Hobbs, P. V., Ross, J. L., Russell, P. B., and Livingstone, J. M.: Properties of aerosols aloft relevant to direct radiative forcing off the mid-Atlantic coast of the United States, J. Geophys. Res., 105, 9859–9885, 2000.

Haywood, J. M. and Shine, K. P.: The effect of anthropogenic sulfate and soot aerosol on the clear sky planetary radiation budget, Geophys. Res. Lett., 22, 603–606, 1995.

Hignett, P., Taylor, J. P., Francis, P. N., and Glew, M. D.: Comparison of observed and modeled direct aerosol forcing during TARFOX, J. Geophys. Res., 104, 2279–2287, 1999.

Holben, B. N., Eck, T. F., Slutker, I., Tanré, D., Buis, J. P., Setzer, A., Vermote, E., Reagan, J. A., Kaufman, Y. J., Nakajima, T., Lavenu, F., Jankowiak, I., and Smirnov, A.: AERONET – A federated instrument network and data archive for aerosol characterization, Remote Sens. Environ., 66, 1–16, 1998.

Holben, B. N., Tanré, D., Smirnov, A., Eck, T. F., Slutsker, I., Abuhassan, N., Newcomb, W. W., Schafer, J. S., Chatenet, B., Lavenu, F., Kaufman, Y. J., Vande Castle, J., Setzer, A., Markham, B., Clark, D., Frouin, R., Halthore, R., Karneli, A., O'Neill, N. T., Pietras, C., Pinker, R. T., Voss, K., and Zibordi, G.: An emerging ground-based aerosol climatology: Aerosol optical depth from AERONET, J. Geophys. Res., 106, 12 067–12 097, 2001.

Horvath, H., Alados Arboledas, L., Olmo, F. J., Jovanović, O., Gangl, M., Kaller, W., Sánchez, C., Sauerzopf, H., and Seidl, S.: Optical characteristics of the aerosol in Spain and Austria and its effect on radiative forcing, J. Geophys. Res., 107, 4386, doi:10.1029/2001JD001472, 2002.

Im, J.-S., Saxena, V. K., and Wenny, B. N.: Temporal trends of black carbon concentrations and regional climate forcing in the southeastern United States, Atmos. Env., 35, 3293–3302, 2001.

Intergovernmental Panel on Climate Change (IPCC), Climate Change 2001, The Scientific Basis, edited by: Houghton, J. T., Ding, Y., Griggs, D. J., Noguer, M., Van der Linden, P. J., and Xiaosu, D., Cambridge Univ. Press, New York, 881 pp., 2001.

Jin, Y., Schaaf, C. B., Woodcock, C. E., Gao, F., Li, X., Strahler, A. H., Lucht, W., and Liang, S.: Consistency of MODIS surface bidirectional reflectance distribution function and albedo retrievals. 2. Validation, J. Geophys. Res., 108, 4159, doi:10.1029/2002JD002804, 2003.

Kiehl, J. T. and Briegleb, B. P.: The relative role of sulfate aerosols and greenhouse gases in climate forcing, Science, 260, 311–314, 1993.

Kim, S.-W., Yoon, S.-C., Jefferson, A., Ogren, J. A., Dutton, E. G., Won, J.-G., Ghim, Y. S., Lee, B.-I., and Han, J.-S.: Aerosol optical, chemical and physical properties at Gosan, Korea during Asian dust and pollution episodes in 2001, Atmos. Environ., 39, 39–50, 2005.

Kim, D.-H., Sohn, B.-J., Nakajima, T., and Takamura, T.: Aerosol radiative forcing over east Asia determined from ground-based solar radiation measurements, J. Geophys. Res., 110, D10S22, doi:10.1029/2004JD004678, 2005.

Kurucz, R. L.: Synthetic infrared spectra, Proceedings of the 154th Symposium of the International Astronomical Union, Tucson, 2–6 March 1992, in: Infrared Solar Physics, edited by: Rabin, D. M., Jefferies, J. T., and Lindsey, C., Kluwer, Dordrecht, The Netherlands, 523–531, 1992.

Lau, K. M., Kim, M. K., and Kim, K. M.: Asian summer monsoon anomalies induced by aerosol direct forcing: The role of the Tibetan Plateau, Clim. Dynam., 26, 855–864, 2006.

Lohmann, U. and Feichter, J.: Global indirect aerosol effects: A review, Atmos. Chem. Phys., 5, 715–737, 2005, http://www.atmos-chem-phys.net/5/715/2005/.

Lucht, W., Schaaf, C. B., and Strahler, A. H.: An algorithm for the retrieval of albedo from space using semiempirical BRDF models, IEEE T. Geosci. Remote, 38, 977–998, 2000.

Mallet, M., Roger, J. C., Depiau, S., Dubovik, O., and Putaud, J.-P.: Microphysical and optical properties of aerosol particles in urban zone during ESCOMPTE, Atmos. Res., 69, 73–97, 2003.

Manktelow, P. T., Mann, G. W., Carslaw, K. S., Spracklen, D. V., and Chipperfield, M. P.: Regional and global trends in sulfate aerosol since the 1980s, Geophys. Res. Lett., 34, L14803, doi:10.1029/2006GL028668, 2007.

Markowicz, K. M., Flatau, P. J., Ramana, M. V., Crutzen, P. J., and Ramanathan, V.: Absorbing Mediterranean aerosols lead to a large reduction in the solar radiation at the surface, Geophys. Res. Lett., 29, 1968, doi:10.1029/202GL015767, 2002.

Markowicz, K. M., Flatau, P. J., Quinn, P. K., Carrico, C. M., Flatau, M. K., Vogelmann, A. M., Bates, D., Liu, M., and Rood, M. J.: Influence of relative humidity on aerosol radiative forcing: An ACE-Asia experiment perspective, J. Geophys. Res., 108, 8662, doi:10.1029/2003JD003066, 2003.

Matsui, T. and Pielke, R. A.: Measurement-based estimation of the spatial gradient of aerosol radiative forcing, Geophys. Res. Lett., 33, L11813, doi:10.1029/2006GL025974, 2006.

Matta, E., Facchini, M. C., Decesari, S., Mircea, M., Cavalli, F., Fuzzi, S., Putaud, J.-P., and Dell'Acqua, A.: Mass closure on the chemical species in size-segregated atmospheric aerosol collected in an urban area of the Po Valley, Italy, Atmos. Chem. Phys., 3, 623–637, 2003,
http://www.atmos-chem-phys.net/3/623/2003/.

Matthias, V., Balis, D., Bösenberg, J., Eixmann, R., Iarlori, M., Komguem, L., Mattis, I., Papayannis, A., Papparlardo, G., Perrone, M. R., and Wang, X.: Vertical aerosol distribution over Europe: Statistical analysis of Raman lidar data from 10 European Aerosol Research Lidar Network (EARLINET) stations, J. Geophys. Res., 109, D18201, doi:10.1029/2004JD004638, 2004.

Mattis, I., Ansmann, A., Wandinger, U., and Müller, D.: Unexpectedly high aerosol load in the free troposphere over central Europe in spring/summer 2003, Geophys. Res. Lett., 30, 2178, doi:10.1029/2003GL018442, 2003.

Mattis, I., Ansmann, A., Müller, D., Wandinger, U., and Althausen, D.: Multiyear aerosol observations with dual-wavelength Raman lidar in the framework of EARLINET, J. Geophys. Res., 109, D13203, doi:10.1029/2004JD004600, 2004.

Mayer, B. and Kylling, A.: Technical Note: The libRadtran software package for radiative transfer calculations – Description and examples of use, Atmos. Chem. Phys., 5, 1855–1877, 2005, http://www.atmos-chem-phys.net/5/1855/2005/.

Mélin, F. and Zibordi, G.: Aerosol variability in the Po Valley analyzed from automated optical measurements, Geophys. Res. Lett., 32, L03810, doi:10.1029/2004GL021787, 2005.

Mélin, F., Clerici, M., Zibordi, G., and Bulgarelli, B.: Aerosol variability in the Adriatic Sea from automated optical field measurements and Sea-viewing Wide Field-of-view Sensor (SeaWiFS), J. Geophys. Res., 111, D22201, doi:10.1029/2006JD007226, 2006.

Meloni, D., di Sarra, A., DeLuisi, J., Di Iorio, T., Fiocco, G., Junkermann, W., and Pace, G.: Tropospheric aerosols in the Mediterranean: 2. Radiative effects through model simulations and measurements, J. Geophys. Res., 108, 4317, doi:10.1029/2002JD002807, 2003.

Menon, S., Hansen, J., Nazarenko, L., and Luo, Y.: Climate effect of black carbon aerosols in China and India, Science, 297, 2250–2253, 2002.

Moody, E. G., King, M. D., Platnick, S., Schaaf, C. B., and Gao, F.: Spatially complete global spectral surface albedos: Value-added datasets derived from Terra MODIS land products, IEEE T. Geosci. Remote, 43, 144–158, 2005.

Moorthy, K. K., Babu, S. S., and Satheesh, S. K.: Aerosol characteristics and radiative impacts over the Arabian Sea during the intermonsoon season: Results from ARMEX field campaign, J. Atmos. Sci., 62, 192–206, 2005.

Nemesure, S., Wagener, R., and Schwartz, S. E.: Direct shortwave forcing of climate by the anthropogenic sulfate aerosol: Sensitivity to particle size, composition, and relative humidity, J. Geophys. Res., 100, 26 105–26 116, 1995.

Norris, J. R. and Wild, M.: Trends in aerosol radiative effects over Europe inferred from observed cloud cover, solar "dimming", and solar "brightening", J. Geophys. Res., 112, D08214, doi:10.1029/2006JD007794, 2007.

O'Neill, N. T., Ignatov, A., Holben, B. N., and Eck, T. F.: The log-normal distribution as a reference for reporting aerosol optical depth statistics: Empirical tests using multi-year, multi-site AERONET sunphotometer data, Geophys. Res. Lett., 27, 3333–3336, 2000.

Perrone, M. R., Santese, M., Tafuro, A. M., Holben, B. N., and Smirnov, A.: Aerosol load characterization over South-East Italy for one year of AERONET sun-photometer measurements, Atmos. Res., 75, 111–133, 2005.

Putaud, J.-P., Van Dingenen, R., and Raes, F.: Submicron aerosol mass balance at urban and semi-rural sites in the Milan area (Italy), J. Geophys. Res., 107, 8198, doi:10.1029/2000JD000111, 2002.

Putaud, J.-P., Raes, F., Van Dingenen, R., Brüggemann, E., Facchini, M.-C., Decesari, S., Fuzzi, S., Gehrig, R., Hüglin, C., Laj, P., Lorbeer, G., Maenhaut, W., Mihalopoulos, N., Müller, K., Querol, X., Rodriguez, S., Schneider, J., Spindler, G., ten Brink, H., Tørseth, K., and Wiedensohler, A.: A European aerosol phenomenology. 2. Chemical characteristics of particulate matter at kerbside, urban, rural and background sites in Europe, Atmos. Environ., 38, 2579–2595, 2004.

Ramanathan, V., Crutzen, P. J., Kiehl, J. T., and Rosenfeld, D.: Aerosols, climate, and the hydrological cycle, Science, 249, 2119–2124, 2001.

Redemann, J., Turco, R. P., Liou, K. N., Hobbs, P. V., Hartley, W. S., Bergstrom, R. W., Browell, E. V., and Russell, P. B.: Case studies of the vertical structure of the direct shortwave aerosol radiative forcing during TARFOX, J. Geophys. Res., 105, 9971–9979, 2000.

Redemann, J., Masonis, S. J., Schmid, B., Anderson, T. L., Russell, P. B., Livingston, J. M., Dubovik, O., and Clarke, A. D.: Clear-column closure studies of aerosols and water vapor aboard the NCAR C-130 during ACE-Asia, 2001, J. Geophys. Res., 108, 8655, doi:10.1029/2003JD003442, 2003.

Remer, L. A. and Kaufman, Y. J.: Dynamic aerosol model: Urban/industrial aerosol, J. Geophys. Res., 103, 13 859–13 871, 1998.

Ricchiazzi, P., Yang, S., Gautier, C., and Sowle, D.: SBDART: A research and teaching software tool for plane-parallel radiative transfer in the Earth's atmosphere, Bull. Am. Meteorol. Soc., 79, 2101–2114, 1998.

Ricchiazzi, P., O'Hirok, W., and Gautier, C.: The effect of NON-Lambertian Surface Reflectance on Aerosol Radiative Forcing, Fifteenth ARM Science Team Meeting Proceedings, Daytona Beach, Florida, USA, 14–18 March, 2005.

Rodríguez, S., Van Dingenen, R., Putaud, J.-P., Dell'Acqua, A., Pey, J., Querol, X., Alastuey, A., Chenery, S., Ho, K.-F., Harrison, R., Tardivo, R., Scarnato, B., and Gemelli, V.: A study on the relationship between mass concentrations, chemistry and number size distribution of urban fine aerosols in Milan, Barcelona and London, Atmos. Chem. Phys., 7, 2217–2232, 2007,
http://www.atmos-chem-phys.net/7/2217/2007/.

Rodríguez, S., Querol, X., Alastuey, A., and de la Rosa, J.: Atmospheric particulate matter and air quality in the Mediterranean: A review, Environ. Chem. Lett., 5, 1–7, 2007.

Roger, J. C., Mallet, M., Dubuisson, P., Cachier, H., Vermote, E., Dubovik, O., and Despiau, S.: A synergetic approach for estimating the local direct aerosol forcing: Application to an urban zone during the Expérience sur Site pour Contraindre les Modèles de Pollution et de Transport d'Emission (ESCOMPTE) experiment, J. Geophys. Res., 111, D13208, doi:10.1029/2005JD006361, 2006.

Rosenfeld, D.: Suppression of rain and snow by urban and industrial air pollution, Science, 287, 1793–1796, 2000.

Rossow, W. B. and Schiffer, R. A.: Advances in understanding clouds from ISCCP, B. Am. Meteorol. Soc., 80, 2261–2287, 1999.

Russel, P. B., Livingstone, J. M., Hignett, P., Kinne, S., Wong, J., Chien, A., Bergstrom, R., Durkee, P., and Hobbs, P. V.: Aerosol-induced radiative flux changes off the United States mid-Atlantic coast: Comparison of values calculated from sunphotometer and in situ data with those measured by airborne pyranometer, J. Geophys. Res., 104, 2289–2307, 1999.

Salomonson, V. V., Barnes, W. L., Maymon, P. W., Montgomery, H. E., and Ostrow, H.: MODIS: Advanced facility instrument for studies of the Earth as a system, IEEE T. Geosci. Remote, 27, 145–152, 1989.

Satheesh, S. K. and Ramanathan, V.: Large differences in tropical aerosol forcing at the top of the atmosphere and Earth's surface, Nature, 405, 60–63, 2000.

Schaaf, C. B., Gao, F., Strahler, A. H., Lucht, W., Li, X., Tsang, T., Strugnell, N. C., Zhang, X., Jin, Y., Muller, J.-P., Lewis, P., Barnsley, M., Hobson, P., Disney, M., Roberts, G., Dunderdale, M., Doll, C., d'Entremont, R. P., Hu, B., Liang, S., Privette, J. L., and Roy, D.: First operational BRDF, albedo nadir reflectance products from MODIS, Remote Sens. Environ., 83, 135–148, 2002.

Sheridan, P. J. and Ogren, J. A.: Observations of the vertical and regional variability of aerosol optical properties over central and eastern North America, J. Geophys. Res., 104, 16 793–16 805, 1999.

Smirnov, A., Holben, B. N., Eck, T. F., Dubovik, O., and Slutsker, I.: Cloud-screening and quality control algorithms for the AERONET database, Remote Sens. Environ., 73, 337–349, 2000.

Smirnov, A., Holben, B. N., Eck, T. F., Slutsker, I., Chatenet, B., and Pinker, R. T.: Diurnal variability of aerosol optical depth observed at AERONET (Aerosol Robotic Network) sites, Geophys. Res. Lett., 29, 2115, doi:10.1029/2002GL016305, 2002.

Sogacheva, L., Hamed, A., Facchini, M. C., Kulmala, M., and Laaksonen, A.: Relation of air mass history to nucleation events in Po Valley, Italy, using back trajectories analysis, Atmos Chem. Phys., 7, 839–853, 2007.

Stamnes, K., Tsay, S. C., Wiscombe, W., and Jayaweera, K.: Numerically stable algorithm for discrete-ordinate-method radiative transfer in multiple scattering and emitting layered media, Appl. Optics, 27, 2502–2509, 1998.

Stern, D. I.: Reversal of the trend in global anthropogenic sulfur emissions, Global Environ. Chang., 16, 207–220, 2006.

Sumanth, E., Mallikarjuna, K., Stephen, J., Moole, M., Vinoj, V., Satheesh, S. K., and Krishna Moorthy, K.: Measurements of aerosol optical depth and black carbon over Bay of Bengal during post-monsoon season, Geophys. Res. Lett., 31, L16115, doi:10.1029/2004GL020681, 2004.

Van Dingenen, R., Raes, F., Putaud, J.-P., Baltensperger, U., Charron, A., Facchini, M.-C., Decesari, S., Fuzzi, S., Gehrig, R., Hansson, H.-C., Harrison, R. M., Hüglin, C., Jones, A. M., Laj, P., Lorbeer, G., Maenhaut, W., Palmgren, F., Querol, X., Rodriguez, S., Schneider, J., Ten Brink, H., Tunved, P., Tørseth, K., Wehner, B., Weingartner, E., Wiedensohler, A., and Wåhlin, P.: A European aerosol phenomenology. 1. Physical characteristics of particulate matter at kerbside, urban, rural and background sites in Europe, Atmos. Environ., 38, 2561–2577, 2004.

Wendling, P., Stifter, A., Mayer, B., Fiebig, M., Kiemle, C., Flentje, H., Wendisch, M., Armbruster, W., Leiterer, U., von Hoyningen-Huene, W., and Petzold, A.: Aerosol-radiation interaction in the cloudless atmosphere during LACE 98. 2. Aerosol-induced solar irradiance changes determined from airborne pyranometer measurements and calculations, J. Geophys. Res., 107, 8131, doi:10.1029/2000JD000288, 2002.

Yu, H., Dickinson, R. E., Chin, M., Kaufman, Y. J., Zhou, M., Zhou, L., Tian, Y., Dubovic, O., and Holben, B. N.: Direct radiative effect of aerosols as determined from a combination of MODIS retrievals and GOCART simulations, J. Geophys. Res., 109, D03206, doi:10.1029/2003JD003914, 2004.

Yu, H., Kaufman, Y. J., Chin, M., Feingold, G., Remer, L. A., Anderson, T. L., Balkanski, Y., Bellouin, N., Bouche, O., Christopher, S., DeCola, P., Kahn, D., Loeb, N., Reddy, M. S., Schulz, M., Takemura, T., and Zhou, M.: A review of measurement-based assessments of the aerosol direct radiative effect and forcing, Atmos. Chem. Phys., 6, 613–666, 2006, http://www.atmos-chem-phys.net/6/613/2006/.

Zhou, M., Yu, H., Dickinson, R. E., Dubovik, O., and Holben, B. N.: A normalized description of the direct effect of key aerosol types on solar radiation as estimated from Aerosol Robotic Network aerosols and Moderate Resolution Imaging Spectroradiometer albedos, J. Geophys. Res., 110, D19202, doi:10.1029/2005JD005909, 2005.